Cooperative Effects Associated with High Electrolyte Concentrations in Driving the Conversion of CO_2 to C_2H_4 on Copper

Shaoyang Lin,[1,9] Yuval Fishler,[2,3,4,9] Soonho Kwon,[5,9] Annette E. Böhme,[6] Weixuan Nie,[1] Matthias H. Richter,[1] Moon Young Yang,[5] Jesse E. Matthews,[7,8] Zachery W. B. Iton,[6] Brian C. Lee,[1] Thomas F. Jaramillo,[7,8] Harry A. Atwater,[6] William A. Goddard III,[5,*] Wilson A. Smith,[2,3,4*] Kimberly A. See[1,10,*]

[1] Division of Chemistry and Chemical Engineering, California Institute of Technology, Pasadena, CA 91125, USA
[2] Department of Chemical and Biological Engineering, University of Colorado, Boulder, CO 80303, USA
[3] Renewable and Sustainable Energy Institute University of Colorado, Boulder, CO 80303, USA
[4] Materials, Chemical, and Computational Science (MCCS) Directorate, National Renewable Energy Laboratory, Golden, CO 80401, USA
[5] Materials and Process Simulation Center, California Institute of Technology, Pasadena, CA 91125, USA
[6] Department of Applied Physics and Material Science, California Institute of Technology, Pasadena, CA 91125, USA
[7] Department of Chemical Engineering, Stanford University, Stanford, CA 94305, USA
[8] SUNCAT Center for Interface Science and Catalysis, SLAC National Accelerator Laboratory, 2575 S and Hill Road, Menlo Park, CA 94025, USA
[9] These authors contributed equally
[10] Lead contact
[*] Correspondence: wag@wag.caltech.edu (W.A.G.) Wilson.Smith@nrel.gov (W.A.S.), ksee@caltech.edu (K.A.S.)

Summary

Increasing the product selectivity and decreasing the cost of product separation is critical for large scale application of electrochemical CO_2 reduction (ECO_2R). We hypothesize that highly concentrated aqueous electrolytes can tune the microenvironment of the catalyst/electrolyte interface and improve product selectivity. Compared to a conventional electrolyte concentration of 1 M HCOOK, the use of a 7.1 M HCOOK electrolyte increases the FE ratio of C_2H_4/CO from 2.2 ± 0.3 to 18.3 ± 4.8 at -1.08 V vs RHE on a Cu gas diffusion electrode. Based on electrochemical analysis and AIMD simulation, the identity and concentration of the cation and anion play more important roles in controlling the CO_2R reaction pathway than the bulk CO_2 solubility and the bulk pH of electrolytes. In-situ ATR-SEIRAS suggests that, unlike 1 M HCOOK, the *CO-bridge binding mode on Cu is dominant in 7.1 M HCOOK electrolyte, which potentially results in less CO release and higher yield of C_2H_4. This study demonstrates that while we can tailor the electrolyte composition to shift product selectivity, the factors that control the product selectivity are numerous and cannot be distilled down into one correlated property-reactivity relationship. Thus, when CO_2R conditions are changed, care must be taken to understand their effects on the bulk electrolyte properties and the electrode-electrolyte interface.

Keywords

CO_2 reduction, Copper electrocatalysis, concentrated electrolyte, product selectivity, electrode-electrolyte microenvironment, adsorbed intermediates

1. Introduction

Electrochemical CO_2 reduction (ECO_2R) provides a promising pathway to produce chemical feedstocks and fuels using a carbon negative method, which is essential for realizing carbon neutrality.[1–7] Despite its intriguing impact on environmental protection, ECO_2R suffers from drawbacks that prevent large-scale deployment.[8–10] Currently, there are a few startup companies targeting conversion of CO_2 to CO, HCOOH, C_2H_4 and other important chemical feedstock materials.[11–15] Among all the technical challenges, reducing the cost of product separation by improving the product selectivity of desired products is one of the obstacles that needs to be addressed.[16–19]

C_2H_4, EtOH, acetate and other C_{2+} products are fundamental chemical feedstock materials that are widely used in chemical industries and can be products of ECO_2R.[6,20] Interestingly, Cu is one of the only heterogeneous catalysts that can form C_{2+} products in ECO_2R.[21–28] Studies have been focused on improving the turnover rate and product selectivity of C_2H_4 and other C_{2+} products in ECO_2R. Specific effort has been made on tuning the microenvironment of the Cu/electrolyte interface to control product selectivity. For instance, strategies to tune the catalytic behavior of Cu metal have been pursued to control its affinity towards intermediates like adsorbed CO (*CO) to lower the C-C coupling energy barrier and inhibit competing reactions. These strategies include tuning the morphology of the electrode surface, modulating the oxidation state, controlling the exposed crystal facets, introducing Cu alloys (e.g. with Ag), or adjusting the interaction between deposited Cu with substrates.[29–35] Additionally, strategies to tune the electrode-electrolyte interface have been pursued that use surface modifiers like ionomer or organic additive films to improve the C_{2+} product turnover rate.[36–41] The films are thought to tune local pH, modify the mass transport of reactants and products, and adjust the interaction of reaction intermediates. Moreover, implementing electrolyte chemistry and tuning the microenvironment of relevant species in solution is also critical to control the product distribution. The choice of solvent and supporting electrolyte can tune the electrolyte properties like pH, buffer capacity, CO_2 solubility, and the mass transport of CO_2, which all play important roles in determining the preference of multiple competing reaction pathway on Cu surface.[42–50]

By tuning the salt concentration, the properties of the electrolyte can be systematically varied. Water-in-salt electrolyte (WiSE) is a type of highly concentrated aqueous electrolyte.[51,52] It was first introduced for achieving the goal of an aqueous battery owing to its wide electrochemical stability window and suitable conductivity.[53,54] The significantly increased salt solubility and decreased concentration of free water of WiSE compared to conventional low concentration electrolyte provides a pathway to tune the electrolyte for CO_2R. As a few studies have shown, applying WiSE for CO_2R can mitigate the unwanted HER reaction and control the product selectivity. The study by Zhang et al. demonstrated that applying LiTFSI WiSE on Au can inhibit HER while promoting CO formation.[55] Meanwhile, Ren et al. proposed that by controlling the surface electric field on electrocatalyst using WiSE, the CO2R product selectivity can be controlled.[56] In another study, Zhang et al. suggested that the reason for $NaClO_4$ WiSE to promote C_{2+} product on Cu is due to the tuning of water activity as a result of the change of the salt concentration.[57] Employing WiSE on Cu for CO_2R alters the Cu/electrolyte interface in multiple ways as per the concentration of cation/anion, the pH, CO_2 mass transport and proton deliver processes all changed simultaneously. Therefore, understanding the effect of changes both in the bulk properties of the electrolyte and the interfacial properties is necessary for fully understanding the impact of WiSE on tuning CO_2R reaction pathway on Cu. Insight will enable the design of optimized WiSE/Cu system to further improve the yield of C_2H_4 and other valuable products.

In this study, we study the effect of electrolyte concentration on CO_2R of a HCOOK supporting electrolyte ranging from 1 M to 7.1 M with a Cu GDE. We find that the high salt concentrations increase the FE ratio of C_2H_4/CO from 2.2 ± 0.3 in the 1 M HCOOK control to 18.3 ± 4.8 in the 7.1 M HCOOK at -1.08 V vs RHE. The origin of the improved product selectivity towards C_2H_4 over CO is investigated from both the perspective of bulk electrolyte properties and interfacial effects at the electrode. As the concentration is increased from 1 M to 7.1 M, both the pH and the solubility of CO_2 are affected. We show, however, that the shift in these two bulk properties cannot fully account for the change in product selectivity. Experimental data supported by ab initio molecular dynamics (AIMD) calculations show that K^+ is an important cation in the 7.1 M electrolyte that is found to stabilize *CO on Cu and facilitate CO-CO coupling. The energy barrier of forming the *OCCO intermediate is lower in 7.1 M HCOOK than 1 M HCOOK, in line with the higher C_2H_4 yield in 7.1 M HCOOK. We also find that the anion can affect the selectivity of C_2H_4 with respect to CO at high electrolyte concentration. To gain more insight into the processes at the interface, the Cu-electrolyte interface is studied using in situ surface-sensitive attenuated reflectance surface enhanced infrared absorption spectroscopy (ATR-SEIRAS). ATR-SEIRAS shows a higher population of the bridge binding *CO ($*CO_B$) in electrolytes with higher salt concentration, highlighting the potential role of $*CO_B$ on Cu in 7.1 M HCOOK on C_2H_4/CO FE ratio. Through the analysis presented here, it becomes clear that the electrolyte concentration changes several factors that range not only from the changes to the bulk electrolyte properties, but also changes to the electrode-electrolyte interface that can affect the C_2H_4/CO ratio. These factors are intertwined, highlighting the complexity of the electrolyte formulation and also the CO_2 reduction reaction, and all come together to change the product distribution.

2. Result and Discussion

2.1. ECO_2R on Cu GDE with HCOOK electrolytes

Aqueous HCOOK is selected as the electrolyte to understand the role of increasing salt concentration on tuning the product selectivity of CO_2R on Cu electrocatalyst. The electrolyte salt is chosen due to the established role of K^+ in affecting CO_2R and varying the concentration allows for a study on the effect of $[K^+]$ on CO_2R.[27,42,58] Later, we find that the $HCOO^-$ is additionally an important component. As the concentration of HCOOK is increased from 1 M to 7.1 M, the concentration of the anions and cations not only increases, but the concentration of water also decreases.[59] The nature of water in the solution changes as high concentrations force coordination of the water to the cations and anions, leaving less "free" water.

We originally hypothesized that the shift in water microenvironment would enable us to change the selectivity of CO_2R products just by changing the salt concentration. To test this hypothesis, electrochemical CO_2 reduction electrolysis is conducted at various HCOOK concentrations in water, up to 9.1 M, and the products are quantified using GC and HPLC. The cathode is a Cu gas diffusion electrode (GDE) fabricated by depositing a 300 nm thick Cu layer on a PTFE gas diffusion layer. Across all concentrations, the products of the reduction include H_2, CH_4, CO, C_2H_4, acetate, 1-propanol, and ethanol, consistent with previous reports of aqueous CO_2R on Cu GDE.[60–62] The quantification of products allows for the determination of the Faradaic efficiency (FE) of each product. Of specific interest here is the ratio of the C_{2+} products, namely C_2H_4, to CO which highlights the ability to form C_2 coupled products over CO. **Figure 1a** shows the ratio of the FE for C_2H_4 to CO as a function of electrolyte concentration and applied potential. As more negative potentials are reached, the amount of C_2H_4 generally increases relative to CO. Interestingly, the ratio of the FE of C_2H_4/CO is also a function of the electrolyte concentration. At the same applied potential with respect to the RHE scale, the FE ratio of C_2H_4/CO increases as the concentration of HCOOK electrolyte increases until 7.1 M HCOOK. Among all screening conditions, the optimal condition that shows highest C_2H_4/CO FE ratio (18.3 ± 4.8) is bias at -1.08 V vs RHE with 7.1 M HCOOK electrolyte. The FE associated with each product and the total current density at these conditions using both a 1 M and 7.1 M electrolyte is shown in **Figure 1b**. In addition to a favorable C_2H_4/CO ratio, the higher concentration electrolyte also yields higher current densities (206.7 ± 23.5 mA/cm^2) and lower FE for parasitic H_2 evolution. The FE for C2H4 at these conditions is 43.0 ± 1.4%. To understand the mechanism that promotes product selectivity towards C_2H_4 over CO, we hereafter compare between 1 M and 7.1 M HCOOK at -1.08 V vs RHE.

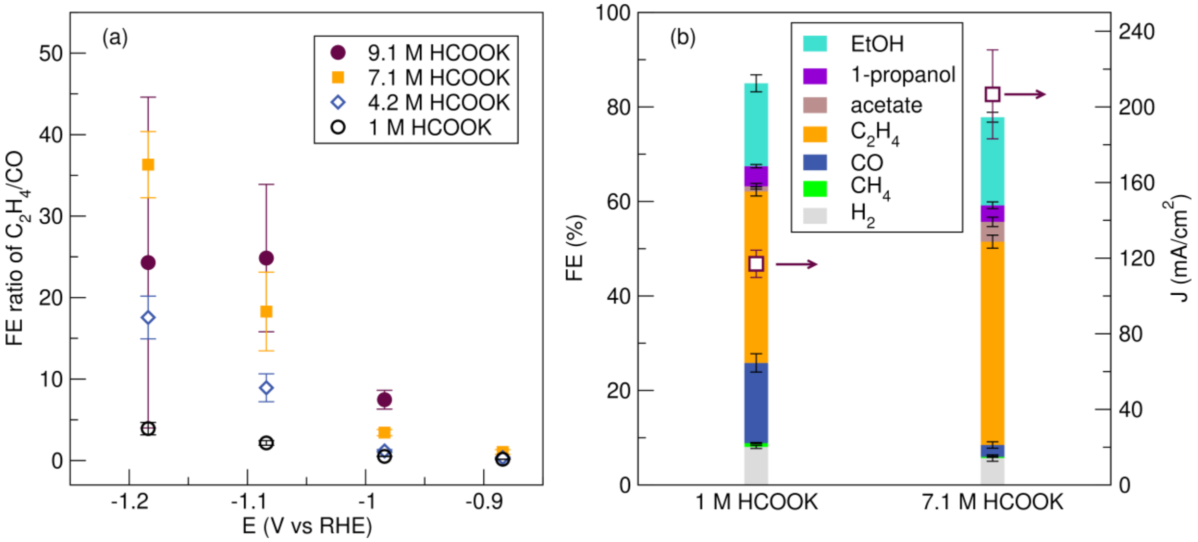

Figure 1. (a) FE ratio of C_2H_4/CO for electrochemical CO_2R on Cu GDE in 1 M, 4.2 M, 7.1 M, and 9.1 M HCOOK under different applied potentials. (b) Product distribution and total current density of electrochemical CO_2R electrolysis on Cu GDE in 1 M HCOOK and 7.1 M HCOOK at -1.08 V vs RHE.

2.2. [CO_2] effect

First, we address the bulk properties that change as the electrolyte concentration increases from 1 M to 7.1 M HCOOK and attempt to vary these properties to determine their effect on the C_2H_4/CO ratio. As the supporting electrolyte concentration increases, both the solubility of CO_2 and the mass transport of CO_2 will be affected, which could explain the C_2H_4/CO ratio shift.[42,63]

First, the solubility of CO_2 is measured in 1 M and 7.1 M HCOOK aqueous solutions by recording the asymmetric stretch mode of CO_2 at 2343 cm^{-1} using attenuated total reflectance – infrared spectroscopy (ATR-IR). The peak area in these electrolytes shown in **Figure S1** is compared to in CO_2 saturated DI water to determine the amount of dissolved CO_2. The CO_2 solubility of 7.1 M HCOOK is determined to be 18 ± 1 mmol/L, while the CO_2 solubility for 1 M HCOOK is 36 ± 2 mmol/L. Lower CO_2 solubility could lead to less local [CO_2] on Cu during electrolysis which would limit the turnover rate of CO_2R and enhance HER. However, the lower CO_2 solubility of 7.1 M HCOOK results in neither lower CO_2R FE nor lower total current density. In fact, recent studies show that slightly lower CO_2 concentrations at GDE can yield higher FE for C_{2+} product.[64–67] We note, however, that it is difficult to correlate the solubility of a reactant to its reactivity at a GDE electrode.

To further probe the effect of [CO_2], the partial pressure of CO_2 delivered to the Cu GDE is tuned by mixing CO_2 and Ar at different ratios at -1.08 V vs RHE. The partial current density associated with H_2, CO, C_2H_4 is plotted vs. the relative [CO_2] in the gas stream in 1 M vs. 7.1 M HCOOK in **Figure 2a and b,** respectively. For both 1 M and 7.1 M HCOOK, as the ratio of CO_2 in the CO_2/Ar mixture increases from 5% to 100%, the partial current density of C_2H_4 and CO increases while the H_2 slightly decreases. Notably, in the 7.1 M HCOOK electrolyte, the partial current density of C_2H_4 increases much more than in the 1 M electrolyte. To gain insight into the selectivity of C_2H_4 vs. CO, the FE associated with each major product and the FE ratio is potted vs. [CO_2] in the gas stream in the 1 M and 7.1 M HCOOK electrolyte in **Figure 2c and d**, respectively. Above 25% CO_2, the FE of C_2H_4 is nearly constant while the FE of H_2 decreases in both electrolytes. The FE for CO in the 1 M electrolyte shows a maximum FE at 75% [CO_2]. The turning point at 75 % CO_2 may be due to the coverage of intermediates, the mass transport, and the competition between aqueous CO_2, $*CO_2^-$ and *CO.[64–66] Conversely, in the FE of CO trends similarly in the 7.1 M electrolyte, but the magnitude of the FE compared to the FE of C_2H_4 remains very low. These factors result in a much higher FE ratio of C_2H_4/CO in the 7.1 M HCOOK electrolyte compared to the 1 M. The FE ratio of C_2H_4/CO generally decreases as the [CO_2] in the gas stream increases.

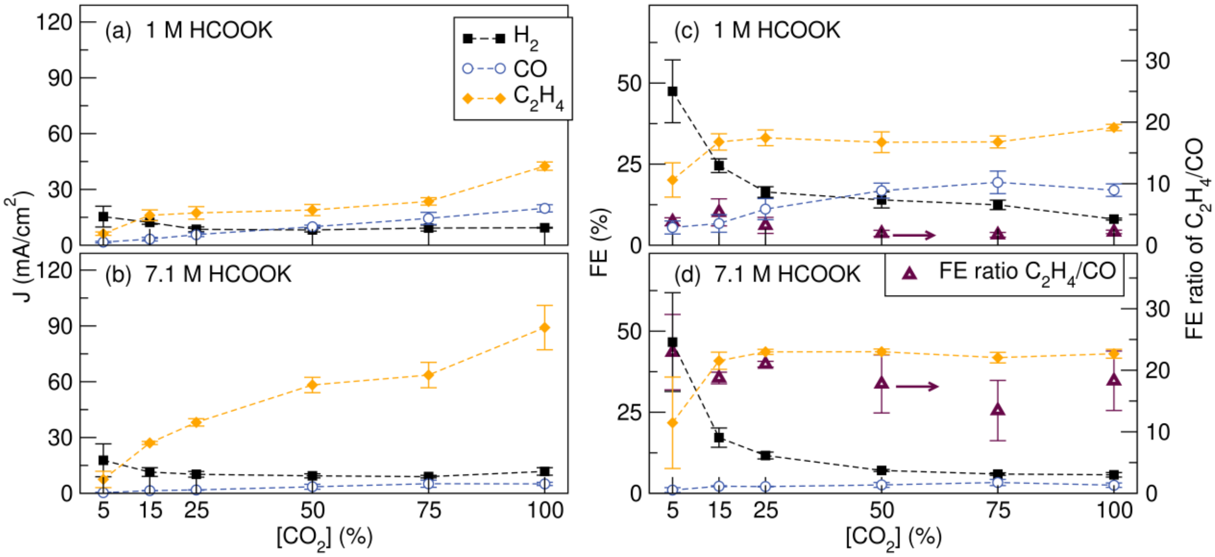

Figure 2. Partial current density of H_2, CO, and C_2H_4 obtained from CO_2R on a Cu GDE as a function of the ratio of CO_2 in CO_2/Ar mixture in the (a) 1 M HCOOK and (b) 7.1 M HCOOK electrolyte at -1.08 V vs RHE. The partial current density of H_2, CO, C_2H_4, and the FE ratio of C_2H_4/CO obtained from CO_2R on Cu GDE in (c) 1 M HCOOK and (d) 7.1 M HCOOK at -1.08 V vs RHE as a function of the ratio of CO_2 in CO_2/Ar mixture.

The FE ratio of C_2H_4/CO in 7.1 M HCOOK at all the [CO_2] are at least 3 times higher than the highest value measured in the 1 M HCOOK electrolyte. The highest partial current for C_2H_4 in 1 M HCOOK is reached at 100 % CO_2, which is similar to the partial current for C_2H_4 in 7.1 M HCOOK at only 25% [CO_2]. Thus, the reactivity of CO_2 is not dependent only on the solubility of CO_2 in the electrolyte at a GDE since the 7.1 M electrolyte has a 50% lower solubility for CO_2. The difference of CO_2 solubility between 1 M and 7.1 M HCOOK cannot explain the origin of the increased C_2H_4/CO FE ratio of 7.1 M HCOOK.

2.3. pH effect

Increasing the concentration of HCOOK electrolytes from 1 M to 7.1 M also increases the bulk pH. Though pH is difficult to measure in these high concentration electrolytes, especially using a pH probe, both a pH probe and pH paper suggest that the pH of 7.1 M HCOOK is approximately 9, which is higher than 1 M HCOOK (pH = 8). The change in bulk pH may change the product selectivity, as nearly all CO_2R products require proton transfers in their generation pathway, and the pH dependent carbonate-bicarbonate equilibrium also affects the local [CO_2]. Higher pH at the electrode surface is known to cause higher yields of C_2 products in CO_2R on Cu electrodes.[44,68–70] The current understanding of the CO_2R mechanism suggests that the rate determining step (RDS) for the C_2 products is C-C bond formation from *CO-*CO or *CO-*COH.[71–76] Though the C-C coupling process is a chemical reaction step which is pH independent, competing reaction pathways like the formation of CH_4 do involve proton transfer and are pH dependent. Higher pH inhibits CH_4 formation, which likely affects the *CO/*COH and possibly other surface species to indirectly promote C-C coupling.[77–79] In the system studied here, higher bulk pH of HCOOK could potentially be a key factor which determines the C_2H_4/CO FE ratio.

To understand the effect of the bulk pH, concentrated KOH (1 mol/L) is titrated into 1 M HCOOK to increase the pH to 9. Electrolysis experiments under the same conditions are conducted using 1 M HCOOK + KOH (pH = 9). Comparing to 1 M HCOOK, the total current density is almost the same: 117.0 ± 10.1 mA/cm^2 for 1 M HCOOK + KOH (pH = 9) and 117 ± 7.2 mA/cm^2 for 1 M HCOOK. By increasing the bulk pH of 1 M HCOOK, the FE of C_2H_4 and the FE ratio of C_2H_4/CO only slightly increase from 36.3 ± 1.0 % and 2.2 ± 0.3 to 37.1 ± 1.7 % and 2.4 ± 0.2, respectively (**Figure S2**). These values are lower than that measured in the 7.1 M HCOOK, demonstrating that the difference of the bulk pH between 1 M and 7.1 M HCOOK is not the key factor that controls the product selection profile, which is consistent with previous results showing that, under the conditions used in this study, bulk pH is not the key factor controlling the CO_2R reaction at the electrode/electrolyte interface.[80]

Though we can control the bulk pH value, the local pH at the electrode surface is significantly different from the bulk pH under CO_2R condition which will play a more significant role in the product profile. To further investigate the role of local pH, in situ confocal fluorescence microscopy is applied to measure the local/surface pH on a Cu GDE under electrolysis conditions.[81–83] By scanning the Z direction within a range of 60 µm of the GDE-electrolyte surface, the approximate location of the electrode-electrolyte interface can be determined. Then, the pH is measured at this location to yield a time dependent pH profile during the first 5 minutes of electrolysis in 1 M HCOOK and 7.1 M HCOOK at -1.08 V vs RHE. Both the pH and the current density during electrolysis are shown in **Figure S3**. Both electrolytes stabilize to a high surface pH, though the 7.1 M HCOOK yields a slightly higher local pH, which could cause shifts in product profiles. However, further work is required to accurately correlate the surface pH measured here with the local pH in the electrochemical double layer to elucidate its impact on product distribution.

2.4. Cation effects:

Besides local pH, the choice of electrolyte can also affect the microenvironment of the reaction sites. According to previous experimental and simulation studies, the major impacts of alkali cation can be described as: (1) stabilizing the reaction intermediates, (2) increasing the electric field in electrochemical double layer and (3) acting as a pH buffer agent at the electrode surface.[84–86] Cations that yield higher C_2 products trend as $Cs^+ > K^+ > Na^+ > Li^+$. Thus, K^+ is suggested to promote C_2 products.[27,42,58] To determine if excess K^+ can account for the product selectivity shift, we select 7.1 M HCOONa electrolyte as a control. Compared to 7.1 M HCOOK, 7.1 M HCOONa decreases the total current density from 206.7 ± 23.5 mA/cm^2

to 56.2 ± 7.3 mA/cm^2 (**Figure 3**). Thus, the partial current density associated with each product also decreases significantly. The FE of C_2H_4, CO, and H_2, however, increase in 7.1 M HCOONa electrolyte, but the FE ratio of C_2H_4/CO decreases by nearly two times. The lower current density along with the lower C_2H_4/CO FE ratio in 7.1 M HCOONa suggests that replacing K^+ with Na^+ inhibits the C-C coupling.

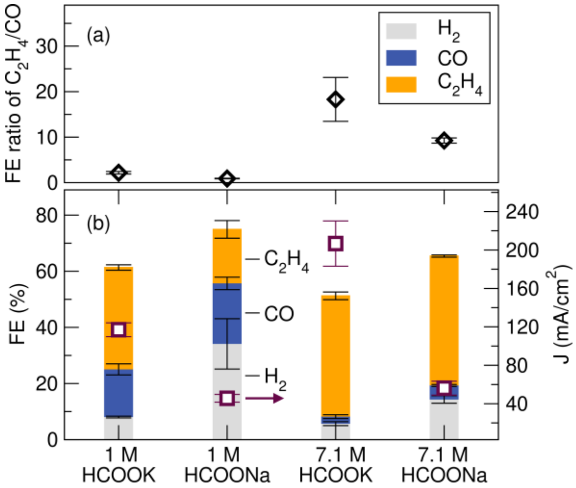

Figure 3. (a) FE ratio of C_2H_4/CO and (b) FE of H_2, CO, and C_2H_4 with the total current density obtained from CO_2R on Cu GDE in 1 M HCOOK, 1 M HCOONa, 7.1 M HCOOK, and 7.1 M HCOONa at -1.08 V vs RHE.

To highlight the effect of K^+ vs. Na^+, we compare the electrolysis results in 1 M HCOOK vs. 1 M HCOONa. Under the same conditions, 1 M HCOONa on Cu GDE dramatically promotes HER relative to the 1 M HCOOK, resulting in higher FE and partial current density for H_2. The total partial current density of C_2H_4 and CO drops by ~44 mA/cm^2 compared to the 1 M HCOOK. Meanwhile, both the FE of C_2H_4 and the FE ratio of C_2H_4/CO decrease. These results suggest that K^+ plays an essential role in promoting the conversion of *CO to C_2H_4.

To understand whether the higher C_2H_4/CO selectivity in the HCOOK electrolytes can be attributed to the increased concentration of K^+, AIMD simulations are conducted to examine the interaction between *CO and K^+, followed by the impact of K^+ on *CO dimerization. First, the equilibrium configuration of the electrolyte-electrode interface is established. The Cu(100)/electrolyte system is equilibrated for 10 ns at 298 K after minimization through CHARMM FF (**Figure S4**). Along the 10 ns trajectory, four snapshots for 7.1 M HCOOK electrolyte system are taken. Those systems are further equilibrated for at least 20 ps with AIMD to get equilibrated potential energies (**Figure S4**). Then, to investigate the influence of K^+ on CO*, four different ensembles of the Cu(100)/7.1 M HCOOK electrolyte system in the presence of *CO are equilibrated (**Figure S5 and S6**) and the average energy over the last 10 ps is calculated. **Figure 4b** and **Table S1** illustrates the relative energies with respect to the corresponding average distance between the oxygen of *CO and K^+. As the distance between *CO and K^+ decreases, the energy also decreases, indicating a significant stabilization of *CO in the presence of adjacent K^+. The explicit interaction results in a system stabilization of 0.5 eV, suggesting that a high molarity of K^+ could lead to increased coverage of *CO or may enhance the conversion of CO_2 to CO.

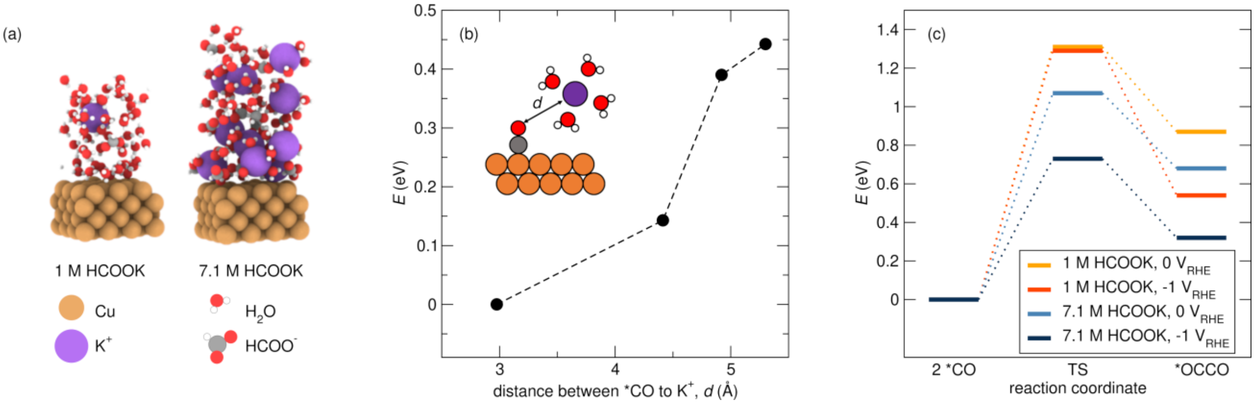

Figure 4. (a) Atomic representation of model systems including 1.0 M and 7.1 M HCOOK with Cu electrode. (b) Relative energies with respect to the average distance between CO* and K^+ for 7.1 M HCOOK/Cu. (c) Energy landscape for CO dimerization under different electrochemical conditions: 1 M / 7.1 M HCOOK at 0 V / -1 V vs RHE.

Previous work suggests that the CO binding must be optimal, not too strong or too weak, for C_{2+} product formation.[28] If *CO binds too weakly, the gas phase CO or formic acid (HCOOH) would be produced as a major product. Conversely, if it binds too strongly, the catalytic surface would be poisoned by *CO. To investigate whether the stabilization of *CO by K^+ leads to CO poisoning or facilitates further *CO-*CO coupling, we conduct metadynamics at room temperature for the CO dimerization step using grand canonical AIMD at fixed potentials of 0 V and -1 V vs RHE in the two different electrolyte concentrations. We construct a potential energy surface (PES) along the distance between two carbon atoms as a collective variable (CV). The time evolution of the CV and the obtained PES are displayed in, **Figure S8** and **Figure 4c**, respectively, and **Table S2** summarizes those results. The reaction free energy of *CO dimerization in 1 M HCOOK can be reduced from 0.87 eV to 0.54 eV by increasing cathodic bias from 0 V to -1 V vs RHE. In 7.1 M HCOOK electrolyte, *CO dimerization is more favorable, decreasing from 0.68 eV to 0.32 eV with the same voltage drop. The corresponding kinetic barrier is also reduced from 1.07 eV to 0.73 eV. Therefore, while a 1 V voltage drop increases the driving force for C-C coupling by 0.3 eV, the high molarity condition further facilitates it by an additional 0.2 eV.

The charge density difference plot (**Figure S9**) of the CO* dimer state (OCCO*) with and without the adjacent K^+ ($d_{CO\text{-}K+}$ = 3.1 Å) shows a strong electronic effect of K^+ for C-C coupling. It shows that the interfacial cation induces the charge (e^-) accumulation on C-C σ bond while it depletes e^- in C-O σ orbital. These effects should reduce the activation barrier for C-C coupling. We also observe charge accumulation on the O p_z orbital of CO* adjacent to the K^+, which might further facilitate its protonation to form OCCOH* the next step along the reduction pathway for forming the C_2 products.[87] Our findings suggest that the higher K^+ concentration both stabilizes CO* and promotes CO dimerization.

2.5. Anion effects:

In addition, the anion can play a role in determining the CO_2R product profile due to specific adsorption on the electrode surface which can induce reconstruction (e.g., halide ion),[48,88,89] shifted buffer capacity that tunes local pH (like HCO_3^-, HPO_4^{2-}),[26,63,67,80] or interaction with surface adsorbed reaction intermediates.[47,48,90,91] To determine if the $HCOO^-$ in particular has an effect on product selectivity in the 7.1 M electrolyte, first we characterize the surface of Cu GDE before and after electrolysis to evaluate the potential of anion adsorption and its impact on the Cu surface (**Figure S10**). The two regions of the XPS that are useful for characterizing $HCOO^-$ are the O 1s and the C 1s regions. In the O 1s region, environments associated with both hydroxide and oxide are present due to the oxidized $Cu(OH)_2$ and Cu_2O/CuO species on the Cu electrode.[92–95] The Cu 2p region suggests the oxidized Cu is mostly Cu(I) due to the lack of satellite peaks characteristic of Cu(II).[93,95] Due to the inevitable air exposure for Cu GDE samples before ex situ XPS measurement, accurate quantification for the ratio of different Cu species is not possible. Nonetheless, it is important to note that there is no significant difference in Cu oxidation state and Cu species on the GDE surface after electrolysis in 1 M HCOOK and 7.1 M HCOOK. Therefore, the shift in product profile is likely not due to the difference in the composition of the Cu GDE surface.

Although no anion adsorption is found via ex situ XPS, in situ $HCOO^-$ adsorption under electrolysis condition is still possible. Therefore, we conduct ex situ X-ray diffraction (XRD) and scanning electron microscopy (SEM) to evaluate the potential Cu surface reconstruction. Ex situ XRD of the Cu GDE before and after electrolysis in 1 M and 7.1 M HCOOK shows no changes (**Figure S11**). However, though Cu reconstruction can penetrate 10-100 nm into the surface and the Cu layer on our GDE is only 300 nm thick, it could be that XRD is not sensitive enough to the surface to observe the reconstruction as it examines the entire 300 nm Cu film.[96–99] In fact, ex situ SEM shows that the morphology of the Cu GDE changes after electrolysis in both 1 M HCOOK and 7.1 M HCOOK, which may affect C_{2+} product yield (**Figure S12**).[96,98–101] The crystallite grains on the Cu surface become less defined after electrolysis in both electrolytes, however, after electrolysis in the 7.1 M HCOOK, the surface has smaller features that are likely small Cu crystallites that could introduce new active sites unique to the 7.1 M electrolyte. This Cu reconstruction could affect the product selectivity. Notably, the morphological change does not increase the electrochemically active surface area (ECSA) after electrolysis in both 1 M and 7.1 M HCOOK (**Table S3**). ECSA has been shown to shift product selectivity.[96,101] Characterization of Cu GDEs under operando condition could illustrate the role morphological evolution on product selectivity but it is out of scope of this study.

To further explore the role of $HCOO^-$, control CO_2R electrolysis experiments are conducted with potassium acetate (KOAc), another type of K^+ based high concentration electrolyte with acetate as the anion. Although a mixture of $HCOO^-$/HCOOH or OAc^-/HOAc can be buffer electrolytes, both HCOOK and KOAc electrolytes should not have strong buffer capacity due to the limited amount of conjugate acid in both electrolytes. Therefore, KOAc is a reasonable choice to compare with HCOOK to analyze the role of $HCOO^-$ in CO_2R. The total current density and FE associated with H_2, CO, and C_2H_4 as a result of CO_2R is measured in 1 M KOAc and is compared to 1 M HCOOK in **Figure 5**. Compared to 1 M HCOOK, no significant change in total current density or product distribution is observed with 1 M KOAc on Cu GDE, suggesting that the CO_2R pathway is similar in both $HCOO^-$ and OAc^- at low electrolyte concentration. Next, we compare 7.1 M KOAc with 7.1 M HCOOK electrolyte to determine if the difference between 7.1 M OAc^- vs. 7.1 M $HCOO^-$ can affect the product distribution. Again, the current density and FE associated with products are shown in **Figure 5**. Compared to 7.1 M HCOOK, running electrolysis with 7.1 M KOAc decreases the total current density from 206.7 ± 23.5 mA/cm^2 to 140.3 ± 11.2 mA/cm^2 and increases the FE ratio of C_2H_4/CO from 18.3 ± 4.8 to 35.7 ± 2.1. The major difference between 7.1 M HCOOK and 7.1 M KOAc is the choice of anion, and thus this result indicates that the role of anion on the product profile is not negligible. Looking back at the AIMD results, however, we do not observe strong electronic interactions of the anions near the surface and OCCO* (**Figure S9b**). Therefore, we postulate that $HCOO^-$ in the outer Helmholtz plane (OHP) or diffusion layer might play important role to modulate the reaction pathway which affects the C_2H_4/CO FE ratio.

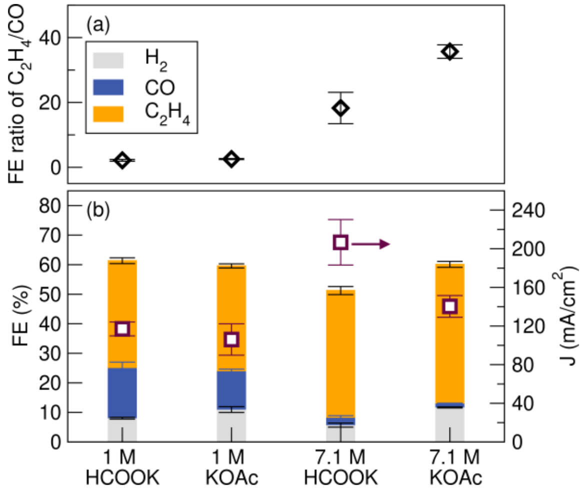

Figure 5. (a) FE ratio of C_2H_4/CO and (b) FE as well as the partial current density of H_2, CO and C_2H_4 obtained from CO_2R on Cu GDE in 1 M HCOOK, 1 M KOAc, 7.1 M HCOOK, and 7.1 M KOAc at -1.08 V vs RHE.

2.6. Probing reaction intermediates on Cu experimentally

The above results suggest that both bulk electrolyte and electrode-electrolyte interface properties are important to control the product profile, however, all surface characterization we have discussed thus far has been limited to theoretical data. To further explore the Cu/HCOOK interface and adsorbed intermediates during ECO_2R experimentally, in situ electrochemical attenuated total reflection – surface enhanced infrared absorption spectroscopy (ATR-SEIRAS) measurements are performed. This technique can help reveal trends in activity and selectivity of adsorbed electrolyte species in a non-invasive approach.

2.6.1. Potential dependent in situ IR

ATR-SEIRAS measurements are limited to the use of a planar (Cu) electrode deposited on an ATR crystal to allow maximum surface enhancement of the IR optical signal. Therefore, it is important to note that the Cu cathode used in the ATR-SEIRAS experiments is in a different architecture than the gas diffusion electrodes used in the above experiments. In particular, the mass transport of CO_2 will be different between the two cells. In the GDE cell, the concentration of CO_2 near the electrode will be much higher as electrolysis proceeds compared to the planar Cu electrode in the ATR-SEIRAS cell, which will quickly consume CO_2 after cathodic bias is applied. Therefore, we focus on analyzing and interpreting the ATR-SEIRAS results at short time scales after electrolysis starts to simulate the high concentration of CO_2 seen in the GDE experiments while the electrolyte is saturated with CO_2.

To determine the effect of CO_2 consumption on the surface speciation in the ATR-SEIRAS cell, we first observe the spectroscopic signal response as a function of time at a fixed potential bias during CO_2R. ATR-SEIRAS allows for IR vibrational modes associated with only those species at or near the surface of the Cu electrode to be detected. To highlight modes associated with species that arrive to the surface as a result of the applied potential, the initial IR spectrum measured at 0.2 V vs RHE is subtracted from those measured after polarization. The difference in the IR spectra are plotted as a function of time after polarization at -0.7 V vs RHE and -1.1 V vs. RHE in the 1 M HCOOK electrolyte in **Figure 6a and b**, respectively. We propose that comparing these two potentials could offer insights on a Cu GDE system since C_2 products are major CO_2R products at -1.1 V vs RHE on Cu while C_1 products are dominant at -0.7

V vs RHE. In 1 M HCOOK, a strong positive peak is observed around 2070 cm^{-1}, a region associated with *CO binding atop to a Cu atom to yield a linear *CO, or *CO$_L$. The frequency range suggests that the *CO$_L$ is a mixture of CO adsorbed on an edge site and/or a defect site, which is termed the high frequency band (HFB). The asymmetric peak shape, which results in having a shoulder at a slightly lower frequencies (around 2058 cm^{-1}) suggests an additional type of *CO$_L$ associated with different Cu sites and is thus termed the low frequency band mode (LFB).[102] Because the signal is positive, it indicates that CO arrives at the surface of the electrode following cathodic polarization. No other *CO signals are observed regardless of the applied potential bias. The negative band around 1650 cm^{-1} corresponds to water bending mode.[103,104] The same *CO$_L$ mode appears at -1.1 V vs. RHE, however, the peak at -0.7 V vs RHE is more pronounced than the signal at -1.1 V vs RHE. Further, the *CO$_L$ observed at -1.1 V is comprised mainly of the lower frequency *CO$_L$, namely LFB. The ratio of the HFB/LFB as a function of time is discussed in more detail in the SI (**Figure S13**). In addition, negative bands are observed within 1420-1590 cm^{-1} at both potentials suggesting desorption of initially adsorbed species. The negative peak around 1380 cm^{-1} is assigned as *HCOO$^-$ in a bidentate orientation since it is absent in a control IR measurement in 0.1 M $KHCO_3$ (**Figure S14**). In addition, a small peak appears around 1408 cm^{-1} only at -1.1 V vs RHE which we assigned to solution phase carbonate (**Figure S15**) species. This is most likely due to the increase in local pH under reducing conditions which results in a shift in equilibrium between bicarbonate and carbonate.[70] Finally, unlike the monotonic decay in *CO$_L$ signal response at -0.7 V vs RHE, polarization at -1.1 V vs. RHE causes the *CO$_L$ peak to first decay over 60 seconds followed by a monotonic slow growth.

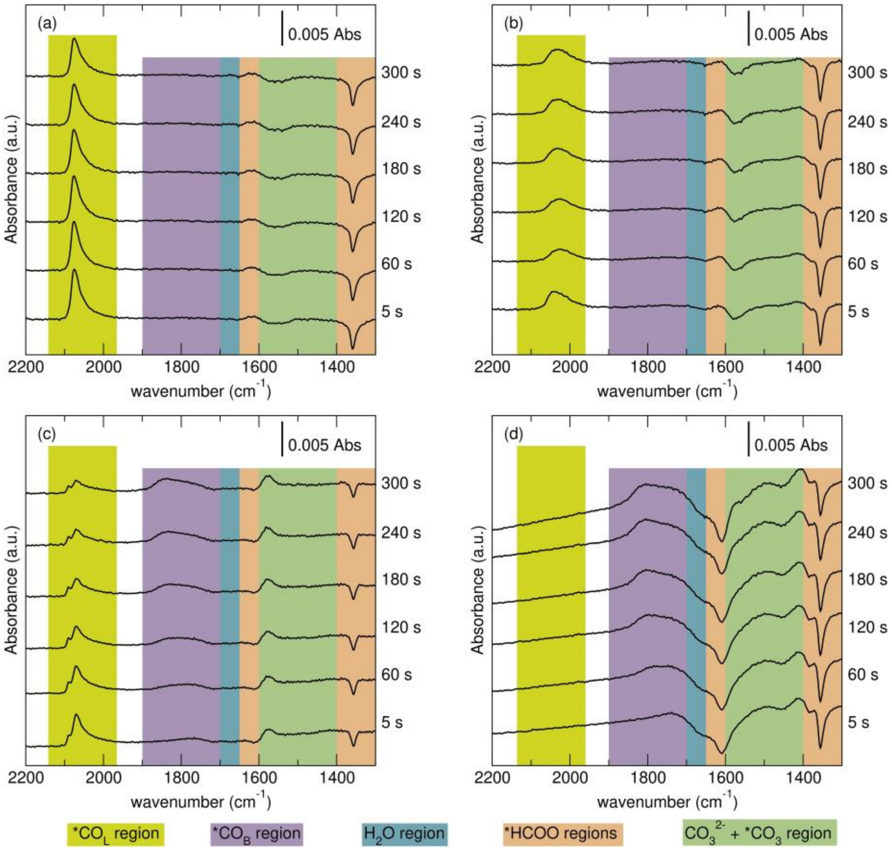

Figure 6. Time evolution CO_2RR ATR-SEIRAS experiment at a potential bias of (a) -0.7 V vs RHE, and (b) -1.1 V vs RHE in 1 M HCOOK and at a potential bias of (c) -0.7 V vs RHE and (d) -1.1 V vs RHE in 7.1 M HCOOK.

Different species and trends are observed in the time evolution ATR-SEIRAS in 7.1 M HCOOK during CO_2R (**Figure 6c and d**). First, a new mode is observed between 1790 - 1850 cm^{-1} associated with *CO between two Cu atoms, termed the bridge bound *CO or $*CO_B$.[105–107] The intensity of the $*CO_B$ grows regardless of potential bias with a faster $*CO_B$ accumulation rate at -1.1 V vs RHE. Similar to 1 M HCOOK, at -0.7 V vs RHE there is a monotonic decay in $*CO_L$. But, in this case, three $*CO_L$ peaks are apparent, with an additional peak at around 2089 cm^{-1} on top of the HFB and LFB. Due to its higher vibrational frequency, this feature most likely results from an adsorbed CO on an additional binding site involving *CO that is bound more weakly to a less coordinated surface site. This adsorbed CO species might exist in 1 M HCOOK but could be hindered by the HFB CO peak. We suspect that the slightly lower value for HFB CO in 7.1 relative to 1 M HCOOK is the result of slightly higher local pH due to higher current density at the same potential bias. It has been proposed by Rebstock et al. that this CO peak is related to the active site for CO_2R to CO.[108] However, their work was performed on Au in 0.1 M bicarbonate solution, and therefore the results might not be translatable to our system so further analysis is needed to compare the different effects of CO binding sites on product selectivity across different catalysts. Moreover, $*CO_L$ is not detected at -1.1 V vs RHE. In addition, an increase in solution phase carbonate (1408 cm^{-1}) and the loss of the water bending mode is recorded at -1.1 V vs RHE. Finally, a growth in the band around 1580 cm^{-1} at -0.7 V vs RHE likely originates from the adsorption of formate, bi/carbonate or CO_2R related species.

The ATR-SEIRAS data clearly show that *CO speciates differently in 1 M vs. 7.1 M HCOOK. In an attempt to directly correlate CO_2R products to the *CO species, we measure the product distribution on a Cu plate electrode in an H-type electrochemical cell were conducted due to its similarity with the *in-situ* IR electrochemical cell. For both electrolytes, the total FE for CO_2R products is higher at -1.1 V vs RHE, but the major product is H_2 (**Table S4**). H_2 is the only significant product in both electrolytes at less negative potential (-0.7 V vs RHE), as well. Therefore, the formation of any *CO reduction product is significantly limited in both the 1 M and the 7.1 M HCOOK electrolytes, making it difficult to correlate surface speciation of *CO to product profiles directly. The 7.1 M HCOOK is particularly hindered by mass transport limitations, as it is more viscous than the 1 M electrolyte, leading to very small quantities of CH_4 and CO product formation in the H-cell. The 1 M electrolyte shows slightly more CH_4, CO, and some C_2H_4, but again the quantities are very small. According to Rebstock et al. when probing CO_2R on Au in 0.1 $MHCO_3$, the highest frequency $*CO_L$ peak was proposed to be related to the active site for CO formation.[108] However, due to the difference between the systems working with Cu in more concentrated solutions using HCOOK as a supporting electrolyte and due to the low CO_2R products according to the H-cell electrolysis, this might not be the case in our system so further investigation is needed. Considering the HFB/LFB ratio, according to Si Young Lee et al. HFB is proposed to be the active species for CO_2R to ethylene.[109] However, according to their results using Raman spectroscopy, there is an increase in HFB signal intensity at -1.1 V vs RHE. In addition, their work was done in 0.1 M $MHCO_3$ which is different than the system probed in our current study.

While the product selectivity profile is different in the GDE and H-cell electrolysis measurements, we attempted to simulate conditions seen in the GDE for further ATR-SEIRAS measurements. For example, in a GDE setup, a concentrated stream of CO_2 is constantly provided to the electrolyte and thus the diffusion layer is much thinner during electrolysis.[110] For the ATR-SEIRAS cell, this condition will be most represented at early time points after starting electrolysis while the electrolyte is saturated with CO_2. Because the time resolution of the ATR-SEIRAS cell is on the order of seconds, we consider the earliest time point of 5 s to be most representative of the highest concentration CO_2 conditions which are closer to the GDE conditions. At moderate potentials (-0.7 V vs. RHE), only $*CO_L$ modes are observed at 1 M HCOOK while both $*CO_L$ and $*CO_B$ modes are observed at 7.1 M HCOOK. If we compare the potential at which C_2 products can form, -1.1 V vs. RHE, only $*CO_L$ modes are observed in the 1 M HCOOK electrolyte and only $*CO_B$ are observed in the 7.1 M HCOOK electrolyte. Previous results showed that the 7.1 M HCOOK electrolyte in the GDE cell has a much higher C_2H_4/CO product selectivity, and we see under similar conditions that $*CO_B$ is the only CO species observed at the Cu surface. Therefore we suggest that the $*CO_B$ species is an important intermediate to promote C-C coupling reactions to yield C_2H_4. The $*CO_B$ grows fastest at -1.1 V vs RHE in 7.1 M HCOOK and is persistent on the surface (**Figure S16**) which might suggest that CO_B is poisoning the surface. However, the exact role of $*CO_B$ is still under debate.[106,111,112]

2.6.2. Mimicking the high current density local environment of a Cu GDE during SEIRAS

To further investigate the effect of *CO binding modes on the CO_2 to C_2H_4 reduction pathways, ATR-SEIRAS was measured under CO reduction conditions at both the as-prepared pH and the KOH adjusted pH (pH~12) for both electrolyte concentrations (**Figure S17a-d**). CO is used in lieu of CO_2 to prevent the formation of carbonate/bicarbonate, which would shift the pH during electrolysis. Increasing the pH of electrolyte offers opportunities to correlate the reaction intermediates measured on Cu at the low current densities achieved in the ATR-SEIRAS batch cell to the ones recorded at the high current density obtained from the electrolysis on GDE. The SEIRAS experiments performed at high pH are meant to mimic the high local pH that develops during CO2R on a GDE when it increases current density from 10's to 100's of mA/cm^2. We note that pH 12 is close to the measured surface pH value discussed earlier, which allows us to assume similar local pH and surface adsorbed intermediates species at Cu GDE.

The ATR-SEIRAS spectra under these conditions are plotted as the potential is stepped from 0 V to -1.2 V vs. RHE using the 1 M HCOOK electrolyte at the as-prepared pH, 7.8, and at an adjusted pH of 11.9 in **Figure S17a and b**. As the cathodic bias is increased, a band around ~2000-2100 cm^{-1} corresponding to $*CO_L$[102,113] first appears then diminishes. The peak intensity is maintained to lower potentials in the pH ~7.8 electrolyte compared to the pH ~11.9 electrolyte. The same experiment is repeated in the 7.1 M HCOOK first at its as-prepared pH of ~9 and then at a KOH adjusted pH of ~11.9 (**Figure S17c and d**). In 7.1 M HCOOK, in addition to a very weak $*CO_L$ peak, the presence of an additional *CO band at lower wavenumbers (1700-1900 cm^{-1}) indicates the formation of $*CO_B$,[102,107] similar to the results from time dependent in situ IR under CO_2 discussed previously. The peak area of $*CO_L$ in 1 M HCOOK is much higher than 7.1 M HCOOK. In both electrolytes, the $*CO_L$ peak emerges at around -0.1 V then diminishes at a more negative potential: -0.9 V for 1 M HCOOK and -0.5 V for 7.1 M HCOOK. The $*CO_B$ peak is observed only in 7.1 M HCOOK where it grows continuously as the applied potential is sweeping catholically with a stark shifting effect. By increasing the pH, the adsorbed CO intensity in both 1 M and 7.1 M HCOOK at native pH is higher than the related *CO peaks in the corresponding KOH adjusted electrolytes at pH 11.9. Because $*CO_B$ is not observed in the 1 M electrolyte at either pH and is observed in the 7.1 M electrolytes at both pHs, we can conclude that the emergence of $*CO_B$ in 7.1 M HCOOK is due to the increased HCOOK concentration and not to the higher pH caused by higher current densities.

It is important to note that the supporting electrolyte concentration does shift the *CO speciation. To test the hypothesis of the supporting electrolyte concentration being a key parameter for CO binding sites distribution during CO_2RR, we measured the ATR-SEIRAS spectral response to an increase in HCOOK concentration under fixed potential bias (**Figure S18**). In doing so, we observe a monotonic displacement between $*CO_L$ and $*CO_B$ as a function of the supporting electrolyte concentration. These results further affirm that the electrolyte concentration plays a major role in the binding sites distribution of adsorbed CO intermediates. Considering the OH stretching region (3000-3700 cm^{-1}) (**Figure S16.b**), we observe a transition from an increase in all water species (1 to 4 hydrogen bonding water species and K^+-H_2O)[114,115]

as well as non-hydrogen bond OH,[116] to a loss in all water species other than "Ice like" (4 hydrogen bonding water species) including non-hydrogen bond OH.

To correlate the surface speciation found in the ATR-SEIRAS measurements to the associated product distribution under similar conditions, the product distribution was measured for a planar Cu electrode during CO reduction in an H-cell. The results are tabulated in **Table S5**. Similar to the results of CO_2R on the planar Cu electrode discussed above, the major product in both electrolyte concentrations at both pHs is again H_2. At low pH conditions, the FE of C_2H_4 in 1 M HCOOK (pH 8) vs. that in 7.1 M HCOOK (pH 9) are very similar, 2.0 ± 0.2 % and 0.94 ± 0.06 %, respectively. The much lower peak area of $*CO_L$ in 7.1 M HCOOK compared to 1 M HCOOK is not correlated to lower yields of C_2H_4. Therefore, even with CO as a C source, we cannot directly corelate the peak area of $*CO_L$ or $*CO_B$ to CO_2R product distribution. At the higher pH condition (pH 12), the FE of C_2H_4 for both electrolyte concentrations is negligible (< 0.2 %), which is not in line with the product distribution measured with the GDE. Thus, even with a high pH that might be correlated with the large current densities measured on a GDE, the low solubility of CO in aqueous electrolyte still limits the mass transport of CO, promoting HER instead. Thus, we cannot directly correlate the *CO speciation on the Cu planar electrode with the product profiles of a Cu GDE.

2.6.3. pH and cation concentration effects on adsorbed CO Stark tuning

Observing the change in vibrational frequency for the C-O stretching mode of *CO could shed insights on the electric field strength in the outer Helmholtz plane (OHP) within the electric double layer which is often referred to as stark tuning.[117,118] It has been previously shown that the electrolyte cation identity (i.e. valence charge and hydration shell radius) affects the CO_L Stark tuning via tuning the width of the OHP.[118,119] In addition, shifts in the vibrational frequency can also result from changes in *CO surface concentrations via dipole-dipole interactions and chemical shifts.[105,120,121] Attempts to deconvolute the apparent Stark tuning have been previously made,[122] but we are unable to isolate the contribution from the applied external electric field. Therefore, our discussion will focus only on the apparent Stark tuning. In addition, this discussion assumes no change in the most stable orientation of *CO species under the effect of applied potential bias, bulk pH value, electrolyte concentration, or changes in surface coverage.

In this work, we sample at least three data points to allow error statistics and reported the apparent Stark tuning using a linear fit (**Figure S17e-h**). In doing so, we find that within each experiment, the Stark tuning increases with an increase in binding energy to the surface, with the largest shift observed for the $*CO_B$ species, followed by the low frequency band (LFB) of $*CO_L$, and then the high frequency band (HFB) of $*CO_L$, (HFB-$*CO_L$ < LFB-$*CO_L$ < $*CO_B$). This is in line with the argument that enhanced π back donation accompanies with an increase in Cu-C coordination, in particular when comparing between $*CO_L$ and $*CO_B$ species where a higher overlap between the frontier orbitals of Cu and CO is suggested.[123–125] Interestingly, apart from a single data point in 1 M HCOOK at pH 11.9 (**Figure S17f**), HFB-CO_L shows a lower population than LFB-$*CO_L$ on the surface. Unlike CO_L, in 7.1 M HCOOK, $*CO_B$'s apparent Stark tuning remains consistent regardless of the bulk pH value (**Figure S17g,h**). Finally, the non-linearity in Stark tuning, and the Stark tuning values for $*CO_L$ between 1 M HCOOK and 7.1 M HCOOK suggest that concentration effects play a major role in the apparent Stark tuning.

As mentioned earlier, due to the concentration effect on the apparent Stark tuning, and since $*CO_L$ is undetectable at higher overpotentials, we are unable to determine the external electric field component effect as a function of K^+ concentration. By comparing apparent Stark tuning of $*CO_L$ within the potential range of (-0.2 V and -0.5 V vs RHE), it appears that there is an increase in the apparent Stark tuning as a function of bulk pH. In addition, the fact that we observed similar apparent Stark tuning in both 1 M HCOOK at pH 11.9 and 7.1 M HCOOK at pH 9.0, while considering an increase in the Stark tuning due to an increase in pH,[126] we suspect that an increase in K^+ concentration from 1 M to 7.1 M also increases the Stark tuning. The lack of linear Stark tunning region for $*CO_L$ in 7.1 M HCOOK at pH 11.9 limits the opportunity to discuss its effect. Nonetheless, based on our results, we propose that both an increase in bulk pH, as well as K^+ concentration increases the apparent Stark tuning, resulting in the following order: 1 M HCOOK (pH 7.8) < 1 M HCOOK (pH 11.9) < 7.1 M HCOOK (pH 9.0) < 7.1M HCOOK (pH 11.9). Previously, it was proposed that when comparing different cations with different identity, an increase in Stark tuning results in an increase in CO_2R activity.[118,119] However, as mentioned above, it has been proposed by Lee et al. that HFB-$*CO_L$ is a more active species for CO_2R to ethylene, while LFB-$*CO_L$ is a more active site for CO formation.[109] They also demonstrated that HFB-$*CO_L$ has a lower Stark tuning rate than LFB-$*CO_L$ which is in agreement with our results discussed above (**Figure S17e-g**). In addition, it has been shown by Rebstock et al. on Au for CO_2R to CO that the active site demonstrates an inverse Stark tuning.[108] However, further analysis at the potential range of interest is required since our analysis is done at lower overpotentials than the electrolysis results. In addition, to our current knowledge, the effect of highly concentrated electrolytes has not been explored previously.

2.6.4. Attempts to bridge the gap between in situ IR measurements and GDE electrolysis

Although the discrepancy observed between the cells used in *in-situ* ATR-SEIRAS and GDE electrolysis cannot be fully resolved, the ATR-SEIRAS measurements still provide valuable information about the *CO binding preference and the properties of $*CO_L$ and $*CO_B$ under different applied potentials, HCOOK concentrations, and bulk pHs. With the results from *in-situ* IR and electrolysis, we propose potential explanations to bridge the gap between *in-situ* IR measurements and CO_2R electrolysis product selectivity on Cu GDE.

The preference of $*CO_B$ on Cu in 7.1 M HCOOK, which results in strongly bound *CO on the surface, could be the reason for less free CO release compared to the 1 M HCOOK electrolyte under GDE conditions. In addition, the mass transport of CO_2 could affect the CO binding site distribution. With higher CO_2 supply rate at the Cu GDE surface, we can assume that more *CO forms on Cu vs. the condition in the H cell. Higher coverage of *CO (potentially both $*CO_L$ and $*CO_B$) may promote a higher C-C coupling rate and produce more C_2H_4. To test this hypothesis, we conducted CO_2R ATR-SEIRAS experiments by sparging the system with a nitrogen balanced 5% CO_2 stream for comparison to the 100% CO_2 stream used in the previous experiments under similar electrolyte concentrations (**Figure S19**). First, we observe that when sparging the electrolyte with 5% CO_2, the modes corresponding to *CO features are less intense. This could be the result of lower CO_2 availability. Importantly, while no $*CO_L$ is observed in 7.1 M HCOOK under 5 % CO_2 polarized between 0.2 to -1.2 V vs. RHE, $*CO_L$ is found on the Cu surface in 7.1 M HCOOK when switching the gas stream to 100 % CO_2 at moderate potentials, around -0.5 to -0.7 V vs. RHE. This suggests that at higher CO_2 mass transport rates, $*CO_L$ is present and measurable on Cu in 7.1 M HCOOK even with the clear preference for the $*CO_B$. Although we do not have direct observation of the *CO binding mode on Cu GDE in this study, the higher CO_2 mass transport in the GDE likely results in more *CO as $*CO_L$ compared to the H cell condition in 7.1 M HCOOK. The potential coupling between $*CO_L$ with $*CO_L$ or $*CO_B$ could facilitate the conversion of *CO to C_2H_4. The overall results can lead to higher FE ratio of C_2H_4/CO in 7.1 M HCOOK than 1 M HCOOK on the Cu GDE.

3. Conclusion

Herein, we find improved selectivity towards C_2H_4 over CO by simply increasing the electrolyte concentration from 1 M to 7.1 M HCOOK on a Cu GDE cathode. We find that both bulk properties of the electrolyte and shifts in speciation at the electrode-electrolyte interface all contribute to the shift in product selectivity. For bulk properties, experimental and simulation results show CO_2 solubility, bulk pH, and the choice and concentration of cation and anion can all change product selectivity. To probe the electrode/electrolyte microenvironment in an attempt to elucidate the CO_2R reaction pathway at the interface, simulations with explicit solvent provide insight into the effect of electrolyte concentration on the *CO and the C-C coupling reaction. Higher HCOOK concentrations allow for more stabilized *CO on Cu likely due to interactions with K^+ and leads to lowered reaction barriers for C-C coupling. Experimental characterization of surface species conducted with *in situ* ATR-SEIRAS reveals that *CO prefers $*CO_B$ sites in the 7.1 M HCOOK vs. the preference for $*CO_L$ sites in the 1 M HCOOK. However, the differences in cell configurations make it difficult to directly correlate the surface adsorbed species to the product profiles. $*CO_B$ may act to suppress the release of CO and promote C_2H_4 formation, but more work needs to be done to prove this correlation. However, $*CO_B$ is certainly the most prominent *CO species in the high concentration electrolyte which strongly suggests that it is not inactive during CO_2R. Thus, this system proves that the intertwined and dynamic effects of various properties ranging from the bulk to the interface should be thoroughly investigated to try to understand CO_2R mechanisms. Although one property could be correlated, it does not mean it is the only property changing to affect a shift in product distribution.

4. Acknowledgements

This work was supported by the Liquid Sunlight Alliance (LiSA), which is supported by the U.S. Department of Energy, Office of Science, Office of Basic Energy Sciences, Fuels from Sunlight Hub under Award Number DE-SC0021266. We gratefully acknowledge the critical support and infrastructure provided for this work by The Kavli Nanoscience Institute at Caltech. We thank the Beckman Institute for their support of the X-Ray Crystallography Facility at Caltech. K.A.S acknowledge support from the David and Lucile Packard Foundation through the Packard Fellowship for Science and Engineering, the Camille & Henry Dreyfus Foundation, and the Alfred P. Sloan Foundation. The XPS data were collected at the Molecular Materials Research Center in the Beckman Institute at Caltech. The authors thank Jake M. Evans for the helpful discussions regarding the XPS data collection. J.M. acknowledges a graduate fellowship through the National Science Foundation Graduate Research Fellowship under grant no. DGE-1656518. This work used expanse at San Diego Supercomputer Center through allocation DMR160114 from the Advanced Cyberinfrastructure Coordination Ecosystem: Services & Support (ACCESS) program, which is supported by National Science Foundation grants #2138259, #2138286, #2138307, #2137603, and #2138296.

5. Author Contribution

S.L. performed electrochemistry experiments. Y.F. conducted in situ ATR-SEIRAS experiments. S.K. and M.Y.Y. performed molecular dynamics simulations. A.E.B. conducted laser-scanning confocal microscopy. W.N. performed NMR test. J.E.M measured CO_2 solubility. Z.W.B.I. collected XRD data. B.C.L performed XPS experiments. T.J., H.A.A., W.A.G., and W.A.S. supervised the project. K.A.S. ideated and supervised the project. All authors analyzed data and prepared the manuscript.

6. Experimental Section

Chemicals

Potassium formate (HCOOK, ReagentPlus®, 99 %) and Potassium trifluoromethanesulfonate, (KOTf, 98 %) were purchased from Sigma Aldrich. Sodium formate (⩾99.0% ACS) is obtained from VWR. Potassium hydroxide (99.98%, trace metal basis) is purchased from Acros Organics. Water was purified by a Nanopure Analytical Ultrapure Water System (Thermo Scientific) or a Milli-Q Advantage A10 Water Purification System (Millipore) with specific resistance of 18.2 MΩ·cm at 25 °C.

Preparation of Cu GDE and Cu plate electrode

A 300 nm thick Cu catalyst layer was deposited on a PTFE gas diffusion layer (Sterlitech, 0.45 micron) using Cu target obtained from Kurt J. Lesker (99.95 %, 2-inch diameter) in ATC Orion 8: Dielectric Sputter System. Cu foil electrode (99.999% trace metals basis, 1 mm thick, purchased from Sigma-Aldrich) was first mechanically polished then electrochemically polished in 1 M H_3PO_4 (85 wt. % in H_2O, 99.99% trace metals basis, purchased from Sigma-Aldrich) under anodic potential for 5 min before electrolysis experiments.

Electrochemical measurements

The electrolysis cell is adapted from the stack flow cell developed by Kuhl et al. (REF, Energy Environ. Sci., 2012, 5, 7050) mentioned previously in literature. Electrochemical measurements were performed on a Biologic SP200 potentiostat under a N_2 atmosphere, using a slice of Cu GDE or Cu plate as the working electrode, leakless Ag/AgCl electrode (EDAQ) as the reference electrode, and Pt foil as the counter electrode with AEM Fumasep FAA-3-50 separating anode cell and cathode cell. The CO_2 or CO_2/Ar mix reactant gas is flowed to the back side of Cu GDE or in electrolyte with Cu plate at a flow rate of 10 sccm. Catholyte and anolyte are circulated at 2.5 ml/min. Electrochemical impedance spectroscopy (EIS) was taken before every measurement to quantify the solution resistance (Rs) for IR correction. The applied potential with the Ag/AgCl scale ($E_{Ag/AgCl}$) RHE was converted to the reversible hydrogen electrode (RHE) scale (E_{RHE}) with the following equation: $E_{RHE} = E_{Ag/AgCl} + 0.059 \times pH + 0.197 + I * Rs$, where i is the current during CO_2R electrolysis. For CO_2 concentration dependent experiment, the partial pressure of CO_2 was controlled by mixing CO_2 and Ar with specific flow rate. Gas mixture with different ratio of CO_2 was flow through the GDE in electrolysis as mentioned previously.

Product quantification

Reactant gas was flowed through the GDE flow cell or H-cell with the flow rate set as 10 sccm by an Alicat flow controller. The gasses passed the electrolysis cell is injected to GC/MS (Agilent 7880A Gas Chromatograph) with Ar as the carrier gas. H2, CO, CH_4, C2H_4 and C_2H_6 was detected by a thermal conductivity detector (TCD) and Flame Ionization detector (FID) and quantified based on calibration curve collected from standard gas samples. The liquid products were quantified by both HPLC (Thermo Scientific Ultimate 3000) and 1H NMR with water suppression technique and Dimethylsulfoxide as internal standard on a Bruker 400 MHz NMR.

Measurement of CO_2 solubility

Measurements of bulk electrolyte were taken using a Nicolet IS30 spectrometer with a VeeMAX^{TM} III (PIKE Technologies) ATR configuration chamber. A custom flow cell was used to allow constant replenishment of CO_2 saturated analyte over a Si ATR Crystal (PIKE Technologies).[127] Reservoirs of DI water, 1M HCOOK, and 7.1 M HCOOK were sparged with CO_2 for 30 minutes prior to measurements and continually sparged with CO_2 while being pumped into the flow cell at 10 mL/min. 32 interferograms were measured for each analyte and the solubility of CO_2 was probed via the area of the asymmetric stretch vibration of CO_2 at 2343 cm^{-1}.[128] Measured CO_2 peak areas in 1 M and 7.1 M HCOOK were obtained by integrating the absorbance between 2333 and 2355 cm^{-1} and then normalized by the CO_2 peak area measured in DI water, which was set to 34 mM.

pH determination

The pH of low concentration electrolytes (≥1 M) is measured by Oakton pH 6+ Handheld Meter. To avoid misreading of the pH of high concentration electrolyte due to uncounted liquid junction potential, pH Test Strips from VWR Chemicals BDH® (pH range: 7.0 to 14.0, pH graduation: 0.5) and EEEE (pH range: 5.0 to 9.0, pH graduation: 0.5) were used to determine to pH value of 4.2 M, 7.1 M and 9.1 M HCOOK.

pH imaging with laser-scanning confocal microscopy

pH imaging experiments were performed with laser-scanning confocal microscopy (CLSM) in combination with the ratiometric fluorescent probe 8-Aminopyrene-1,3,6-trisulfonic acid trisodium salt (APTS) purchased from Millipore Sigma that acts as an excited-state fluorescence sensor of the local pH. APTS can directly sense local hydroxide activity and is sensitive to a pH range between 11.7 and 14. 200 µM APTS were dissolved in 1 M and 10 M CO_2-saturated HCOOK electrolyte, respectively. A custom-made electrochemical cell compatible with CLSM was used to map the local pH value at an applied potential of -1.7 V vs. Ag/AgCl as a function of time. The pH was mapped in an area of 443 µm x 443 µm with a resolution of 64 x 64 pixels parallel to the electrode surface. In the direction perpendicular to the electrode surface, the pH was imaged over a range of 61 µm with a step size of 1 µm, starting a few microns below the surface. The pH value was averaged for each z-position and the plane with the highest average pH value was assumed to represent the pH at the position closest to the electrode surface since the pH increases as a function of proximity to the cathode surface.

Ex situ characterization of Cu GDE

X-ray photo-electron spectroscopy (XPS) data were collected using a Kratos AXIS Ultra spectrometer (Kratos Analytical, Manchester, UK) equipped with a monochromatic Al $K\alpha_1$ X-ray source (1486.7 eV). Data were collected at pressures of ~$5x10^{-9}$ Torr. The electron-collection lens aperture was set to sample a 700x300 µm spot. The survey scan was collected with an analyzer pass energy of 40, with a step size of 1 eV and a dwell time of 100 ms. The element-specific scans were collected with an analyzer pass energy of 20, a step size of 0.05 eV, and a dwell time of 100 ms. The instrument energy scale and work function were calibrated using clean Au, Ag, and Cu standards. All spectra were collected with no external charge neutralization with the exception of the blank Cu GDE sample, which was collected with an electron gun charge neutralizer with a charge balance voltage of 1.5 V. The spectra were referenced with the adventitious carbon peak shifting to 284 eV. The instrument was operated by Vision Manager software version 2.2.10 revision 5. The XPS data were analyzed using CasaXPS software (CASA Software Ltd).

(Acknowledgement: The XPS data were collected at the Molecular Materials Research Center in the Beckman Institute at Caltech. The authors thank Jake M. Evans for assistance with XPS data collection.)

Powder X-ray Diffraction (PXRD) data were collected using a Rigaku SmartLab diffractometer (Cu Kα). The patterns of all samples and blank were collected using Bragg-Brentano geometry, from 10° to 60° 2θ with a step size of 0.03° and a rate of 10° per minute. Scanning Electron Microscope (SEM) images were recorded with a NOVA NanoSEM 450 using 10 kV accelerating voltage and spot size of 3.

In situ ATR-SEIRAS

For *in-situ* ATR-FTIR measurements, a Nicolet 6700 FTIR spectrometer (Thermo Fisher Scientific) with VeeMAX^{TM} III (PIKE Technologies) ATR configuration chamber was used. The photoelectrochemical experiments were performed in a J1W Jackfish spectro-electrochemical cell (PIKE Technologies) with a

PTFE/PEEK base, and IRUBIS Si(100) specialized 1 ATR element (single-bounce ATR crystal). Polycrystalline Au electrodes were chemically deposited (electroless deposition) based on previous works, which was first established and demonstrated by Osawa in 2002.[129] Each electrode was first deaired with argon for at least 2 minutes per ml of electrolyte, then cycled between 0.2 V – 1.75 V vs RHE using a gold mesh as a counter electrode for 10 cycles at 50 mV/s for surface cleaning and SEIRA activation.

Following Au SEIRA activation, Cu catalyst synthesis was conducted by electrodeposition via direct cathodic electro-reduction within a modified electrochemical ATR-FTIR cell. The cell assembly consists of the same base piece from the ATR-FTIR PTFE/PEEK with an in lab made acrylic top piece, which attaches to the PTFE/PEEK base and contains a bubbler, reference electrode, and counter electrode ports. The counter electrode was held in parallel to the working electrode directly above it. A graphite rod was used as the counter electrode and Ag/AgCl electrode was used as the reference electrode. As a precursor, 5.75 mM copper sulfate pentahydrate ($CuSO_4 \cdot 5H_2O$, 99.995% trace metals basis, Sigma-Aldrich) in 0.1 M Sulfuric acid (H_2SO_4 - Merck, Suprapur 96%), similar to Heyes et al.,[130] was used deposited at a potential bias of 59 mV vs RHE for a total charge of 44 mC/cm^2_{geo}. Post electrodeposition, electrocatalyst was rinsed with pH~9.2 KOH (Semiconductor grade pellets, 99.99% trace metals basis, Sigma-Aldrich) solution 3 times followed by 3 rinses with analyte (either 1 M or 7.1 M - HCOOK, ReagentPlus®, 99%, Sigma-Aldrich).

Prior to electrochemical (EC) ATR-SEIRAS experiments the analyte solution was deaired with argon for at least 2 minutes per ml of solution. After this, a potential bias was applied for 5 minutes to reduce the copper oxide, at the copper oxide reduction peak potential (~0 V vs RHE). For pH-controlled experiments, the solution was CO spurged for at least 2 minutes per ml of solution with continuous bubbling throughout the experiment. Then, a background spectrum was taken at 0.0 V vs RHE averaging over 32 interferograms followed by a potential step series with increments of -0.1 V between 0.0 V and -1.2 V vs RHE while collecting 32 interferograms at each potential step. For time evolution EC ATR-SEIRAS experiments, a background spectrum was taken at 0.2V vs RHE, averaging over 32 interferograms followed by a potential step to either -0.7 or -1.1 V vs RHE collecting 64 interferograms per time stamp. For CO_2 reduction time evolution experiments, the solution was CO_2 spurge for at least 2 minutes per ml of solution with continuous bubbling throughout the experiment. Lastly, for in situ CO_2RR EC ATR-SEIRAS experiments, a background spectrum was taken at 0.2 V vs RHE, averaging over 32 interferograms followed by a cyclic voltammetry (CV) sweep between 0.2 and -1.2 V vs RHE. During the CV, 17 interferograms were collected over the course of 10 seconds (10 mV intervals). Finally, data has been averaged out collecting 170 interferograms over 100 mV intervals.

Computational Methods

The initial structures were modeled using the CHARMM-GUI *Nanomaterial Modeler*.[131,132] Each model comprised one CO molecule and either one pair or ten pairs of K^+ and $HCOO^-$ ions, representing 1 M or 7.1 M concentrations, respectively, with 56 H_2O on top of 4 layers of $3\sqrt{2} \times 3\sqrt{2}$ Cu(100). Classical molecular dynamics simulations were performed to equilibrate the constructed systems using GROMACS[133] with a 2 fs timestep. We employed the CHARMM force field[134], and the water molecules were described by the TIP3P model[135]. Initially, the constructed models were relaxed by steepest-descent energy minimization, followed by equilibration in the NVT ensemble (constant particles, constant volume, and 298 K temperature) for 100 ps, where positional restraints were applied on the CO molecule and the Cu layers with a force constant of 1 eV $Å^{-2}$. For each system, we additionally performed 10 ns NVT simulations at 298 K without any restraints for further equilibration. The temperature was controlled using a velocity-rescale thermostat with a damping constant of 1.0 ps[136], and periodic boundary conditions were applied in all three directions.

The Vienna ab initio simulation package (VASP ver. 5.4.5)[137] was used for DFT calculations. Electron exchange and correlation were treated within the generalized gradient approximation (GGA)[138] in the form of the PBE functional, including the D3 correction for London Dispersion (van der Waals attraction).[139] The interaction between the ionic core and the valence electrons was described by the projector-augmented wave (PAW) method.[140] The plane-wave basis set was truncated with an energy cutoff of 500 eV and the Brillouin zone was sampled only at gamma point. The electronic structure was minimized until the total energy converges to 10^{-5} eV. Our model systems employed $3\sqrt{2} \times 3\sqrt{2}$ Cu(100) with 4 Cu layers with the top layer equilibrated while the atoms of the other 3 layers were fixed. The system explicitly includes 1 and 10 K^+ and $HCOO^-$ pairs with 56 H_2O to mimic 1 M and 7.1 M HCOOK electrolyte, respectively (**Figure S4**). Finite temperature ab-initio molecular dynamics (AIMD) was, then, performed for 20 ps to equilibrate the systems at room temperature. The canonical ensembles (NVT) were equilibrated at 298 K using the Nose-Hoover thermostat[141,142] with 1 fs time step and 40 fs damping parameter.

The implicit electrolyte based on Poisson-Boltzmann model is included using VASPsol[143] to neutralize the system with some net charge (non-zero) for grand canonical dynamics. To prevent the fictitious implicit electrolyte inclusion in explicit solvent regime, we used SOLHYBRID (explicit-implicit solvent model)[144] which employs a modified shape function with parameter of σ_{SH} = 1 Å and α_{SH} = 10 %. This effectively removes the bound charge in the explicit region, as shown in **Figure S5**. For constant potential dynamics with a finite temperature, we used the TPOT routine[144] which guides the electrode to a target potential by varying the number of electrons. The number of electrons was optimized for each ionic step when the potential deviation was larger than a threshold of 0.01 V with a rate limit of 0.2 V/electron. This setup allows the system reach to the target potential within 200 fs (**Figure S7**).

To obtain the kinetic barrier of the CO dimerization step, a metadynamics simulation[145] was performed using the last atomic configuration and velocities from the > 15 ps equilibration at each electrochemical condition. The collective variable (CV) was defined as the atomic C distance of two surface-bound CO (CO*). The initial structures including the atomic configurations and velocities and predictor-corrector coordinates for the four systems, 1 M HCOOK (at 0 V vs RHE), 1 M HCOOK (at -1 V vs RHE), 7.1 M HCOOK (at 0 V vs RHE), 7.1 M HCOOK (at -1 V vs RHE) are provided (**Figure S8**). A time-dependent bias potential was applied with 20 fs time intervals using a Gaussian height (h) of 0.05 eV and width (w) of 0.10 eV. To prevent the two CO* from diffusing away from each other, a single Gaussian hill with h = 4.5 eV and w = 0.2 eV was applied to guide the metadynamics not to exceed the CV = 5 Å as a limit. The dynamics was stopped when the CV exceed the limit, which occurred after 25 ps. The potential energy surface (PES) was calculated by adding the Gaussian potential in a one-dimensional grid ranging from 1 Å to 7 Å with 1000 intervals.

The vibrational density of states (vDoS) was calculated using the 2PT method with the last 10 ps of trajectory from the room-temperature equilibration.[146]

The equilibration procedures in the presence of a single *CO using PBE-D3 leads to the vDoS of CO* stretching mode ranging from 1400~1550 cm^{-1}, which is much lower than experimental values.[102,147,148] This observation is attributed to the hollow CO preference of the PBE-D3 level of theory[149] due to a substantial π backdonation from Cu d-band to the 2π* orbital of CO, originating from the underestimated LUMO (2π*) level of CO molecule.[150] To address this issue, the rotationally variant DFT+U method has been proposed.[151] But, this method may encounter challenges in accurately describing the frustrated rotational motion of CO* during room temperature equilibration or the energy configuration along CO dimerization, as discussed later in this study. Alternatively, the hybrid functional incorporating a fraction of exact exchange can correctly predict the site preferences by mitigating the self-interaction.[152–154] However, the dynamics with this high level of theory is practically prohibitive even with the hybrid method with a periodic LCAO DFT code. Even so, the current level of theory furnishes valuable insights into surface-adsorbate-electrolyte interactions at a computational cost suitable for full explicit dynamics.

7. References

(1) Resasco, J.; Bell, A. T. Electrocatalytic CO2 Reduction to Fuels: Progress and Opportunities. *Trends in Chemistry* **2020**, *2* (9), 825–836. https://doi.org/10.1016/j.trechm.2020.06.007.

(2) Fan, L.; Xia, C.; Yang, F.; Wang, J.; Wang, H.; Lu, Y. Strategies in Catalysts and Electrolyzer Design for Electrochemical CO2 Reduction toward C2+ Products. *Science Advances* **2020**, *6* (8), eaay3111. https://doi.org/10.1126/sciadv.aay3111.

(3) Xia, R.; Overa, S.; Jiao, F. Emerging Electrochemical Processes to Decarbonize the Chemical Industry. *JACS Au* **2022**. https://doi.org/10.1021/jacsau.2c00138.

(4) Gary Grim, R.; Huang, Z.; T. Guarnieri, M.; R. Ferrell, J.; Tao, L.; A. Schaidle, J. Transforming the Carbon Economy: Challenges and Opportunities in the Convergence of Low-Cost Electricity and Reductive CO 2 Utilization. *Energy & Environmental Science* **2020**, *13* (2), 472–494. https://doi.org/10.1039/C9EE02410G.

(5) Masel, R. I.; Liu, Z.; Yang, H.; Kaczur, J. J.; Carrillo, D.; Ren, S.; Salvatore, D.; Berlinguette, C. P. An Industrial Perspective on Catalysts for Low-Temperature CO2 Electrolysis. *Nat. Nanotechnol.* **2021**, *16* (2), 118–128. https://doi.org/10.1038/s41565-020-00823-x.

(6) Huang, Z.; Grim, R. G.; Schaidle, J. A.; Tao, L. The Economic Outlook for Converting CO2 and Electrons to Molecules. *Energy Environ. Sci.* **2021**. https://doi.org/10.1039/D0EE03525D.

(7) Sheehan, S. W.; Buonsanti, R. Deriving Value from CO2: From Catalyst Design to Industrial Implementation. *Chem Catalysis* **2021**, *1* (4), 751–753. https://doi.org/10.1016/j.checat.2021.08.010.

(8) Zhang, S.; Fan, Q.; Xia, R.; Meyer, T. J. CO2 Reduction: From Homogeneous to Heterogeneous Electrocatalysis. *Acc. Chem. Res.* **2020**, *53* (1), 255–264. https://doi.org/10.1021/acs.accounts.9b00496.

(9) Liang, S.; Altaf, N.; Huang, L.; Gao, Y.; Wang, Q. Electrolytic Cell Design for Electrochemical CO2 Reduction. *Journal of CO2 Utilization* **2020**, *35*, 90–105. https://doi.org/10.1016/j.jcou.2019.09.007.

(10) Goldman, M.; Prajapati, A.; Duoss, E.; Baker, S.; Hahn, C. Bridging Fundamental Science and Applied Science to Accelerate CO2 Electrolyzer Scale-Up. *Current Opinion in Electrochemistry* **2023**, *39*, 101248. https://doi.org/10.1016/j.coelec.2023.101248.

(11) *Meet Twelve, The Carbon Transformation Company™*. Twelve. https://www.twelve.co (accessed 2024-06-02).

(12) *AIR COMPANY | Carbon Technology Leader for a Decarbonized Future*. AIR COMPANY. https://www.aircompany.com/ (accessed 2024-06-02).

(13) *Converting Carbon. Storing Energy.* OCOchem. https://ocochem.com/ (accessed 2024-06-02).

(14) *Dioxycle | Rethinking emissions and displacing fossil fuels*. https://dioxycle.com/ (accessed 2024-06-02).

(15) *Oxylus Energy - A circular economy for a zero-emission Earth*. Oxylus Energy. https://oxylusenergy.com/ (accessed 2024-06-02).

(16) Xia, C.; Zhu, P.; Jiang, Q.; Pan, Y.; Liang, W.; Stavitski, E.; Alshareef, H. N.; Wang, H. Continuous Production of Pure Liquid Fuel Solutions via Electrocatalytic CO2 Reduction Using Solid-Electrolyte Devices. *Nat Energy* **2019**, *4* (9), 776–785. https://doi.org/10.1038/s41560-019-0451-x.

(17) Alerte, T.; Edwards, J. P.; Gabardo, C. M.; O'Brien, C. P.; Gaona, A.; Wicks, J.; Obradović, A.; Sarkar, A.; Jaffer, S. A.; MacLean, H. L.; Sinton, D.; Sargent, E. H. Downstream of the CO2 Electrolyzer: Assessing the Energy Intensity of Product Separation. *ACS Energy Lett.* **2021**, *6* (12), 4405–4412. https://doi.org/10.1021/acsenergylett.1c02263.

(18) Kibria Nabil, S.; McCoy, S.; Kibria, M. G. Comparative Life Cycle Assessment of Electrochemical Upgrading of CO $_2$ to Fuels and Feedstocks. *Green Chem.* **2021**, *23* (2), 867–880. https://doi.org/10.1039/D0GC02831B.

(19) Moore, T.; Oyarzun, D. I.; Li, W.; Lin, T. Y.; Goldman, M.; Wong, A. A.; Jaffer, S. A.; Sarkar, A.; Baker, S. E.; Duoss, E. B.; Hahn, C. Electrolyzer Energy Dominates Separation Costs in State-of-the-Art CO2 Electrolyzers: Implications for Single-Pass CO2 Utilization. *Joule* **2023**, *7* (4), 782–796. https://doi.org/10.1016/j.joule.2023.03.015.

(20) De Luna, P.; Hahn, C.; Higgins, D.; Jaffer, S. A.; Jaramillo, T. F.; Sargent, E. H. What Would It Take for Renewably Powered Electrosynthesis to Displace Petrochemical Processes? *Science* **2019**, *364* (6438), eaav3506. https://doi.org/10.1126/science.aav3506.

(21) Chen, Y.; Miao, R. K.; Yu, C.; Sinton, D.; Xie, K.; Sargent, E. H. Catalyst Design for Electrochemical CO2 Reduction to Ethylene. *Matter* **2024**, *7* (1), 25–37. https://doi.org/10.1016/j.matt.2023.12.008.

(22) Karapinar, D.; Creissen, C. E.; Rivera de la Cruz, J. G.; Schreiber, M. W.; Fontecave, M. Electrochemical CO2 Reduction to Ethanol with Copper-Based Catalysts. *ACS Energy Lett.* **2021**, *6* (2), 694–706. https://doi.org/10.1021/acsenergylett.0c02610.

(23) Heenen, H. H.; Shin, H.; Kastlunger, G.; Overa, S.; Gauthier, J. A.; Jiao, F.; Chan, K. The Mechanism for Acetate Formation in Electrochemical CO(2) Reduction on Cu: Selectivity with Potential, pH, and Nanostructuring. *Energy Environ. Sci.* **2022**, *15* (9), 3978–3990. https://doi.org/10.1039/D2EE01485H.

(24) Chen, J.; Wang, T.; Li, Z.; Yang, B.; Zhang, Q.; Lei, L.; Feng, P.; Hou, Y. Recent Progress and Perspective of Electrochemical CO2 Reduction towards C2-C5 Products over Non-Precious Metal Heterogeneous Electrocatalysts. *Nano Res.* **2021**, *14* (9), 3188–3207. https://doi.org/10.1007/s12274-021-3335-x.

(25) Garza, A. J.; Bell, A. T.; Head-Gordon, M. Mechanism of CO2 Reduction at Copper Surfaces: Pathways to C2 Products. *ACS Catal.* **2018**, *8* (2), 1490–1499. https://doi.org/10.1021/acscatal.7b03477.

(26) Hori, Y.; Murata, A.; Takahashi, R. Formation of Hydrocarbons in the Electrochemical Reduction of Carbon Dioxide at a Copper Electrode in Aqueous Solution. *J. Chem. Soc., Faraday Trans. 1* **1989**, *85* (8), 2309. https://doi.org/10.1039/f19898502309.

(27) Nitopi, S.; Bertheussen, E.; Scott, S. B.; Liu, X.; Engstfeld, A. K.; Horch, S.; Seger, B.; Stephens, I. E. L.; Chan, K.; Hahn, C.; Nørskov, J. K.; Jaramillo, T. F.; Chorkendorff, I. Progress and Perspectives of Electrochemical CO2 Reduction on Copper in Aqueous Electrolyte. *Chem. Rev.* **2019**, *119* (12), 7610–7672. https://doi.org/10.1021/acs.chemrev.8b00705.

(28) Bagger, A.; Ju, W.; Varela, A. S.; Strasser, P.; Rossmeisl, J. Electrochemical CO2 Reduction: A Classification Problem. *ChemPhysChem* **2017**, *18* (22), 3266–3273. https://doi.org/10.1002/cphc.201700736.

(29) Luc, W.; Fu, X.; Shi, J.; Lv, J.-J.; Jouny, M.; Ko, B. H.; Xu, Y.; Tu, Q.; Hu, X.; Wu, J.; Yue, Q.; Liu, Y.; Jiao, F.; Kang, Y. Two-Dimensional Copper Nanosheets for Electrochemical Reduction of Carbon Monoxide to Acetate. *Nat Catal* **2019**, *2* (5), 423–430. https://doi.org/10.1038/s41929-019-0269-8.

(30) Gao, D.; Arán-Ais, R. M.; Jeon, H. S.; Roldan Cuenya, B. Rational Catalyst and Electrolyte Design for CO2 Electroreduction towards Multicarbon Products. *Nat Catal* **2019**, *2* (3), 198–210. https://doi.org/10.1038/s41929-019-0235-5.

(31) Lin, Y.-R.; Lee, D. U.; Tan, S.; Koshy, D. M.; Lin, T. Y.; Wang, L.; Corral, D.; Avilés Acosta, J. E.; Zamora Zeledon, J. A.; Beck, V. A.; Baker, S. E.; Duoss, E. B.; Hahn, C.; Jaramillo, T. F. Vapor-Fed Electrolyzers for Carbon Dioxide Reduction Using Tandem Electrocatalysts: Cuprous Oxide Coupled with Nickel-Coordinated Nitrogen-Doped Carbon. *Advanced Functional Materials* **2022**, *32* (28), 2113252. https://doi.org/10.1002/adfm.202113252.

(32) Sedighian Rasouli, A.; Wang, X.; Wicks, J.; Dinh, C.-T.; Abed, J.; Wu, F.-Y.; Hung, S.-F.; Bertens, K.; Huang, J. E.; Sargent, E. H. Ga Doping Disrupts C-C Coupling and Promotes Methane Electroproduction on CuAl Catalysts. *Chem Catalysis* **2022**. https://doi.org/10.1016/j.checat.2022.03.016.

(33) Wu, Y.; Chen, C.; Yan, X.; Wu, R.; Liu, S.; Ma, J.; Zhang, J.; Liu, Z.; Xing, X.; Wu, Z.; Han, B. Enhancing CO 2 Electroreduction to CH 4 over Cu Nanoparticles Supported on N-Doped Carbon. *Chemical Science* **2022**, *13* (28), 8388–8394. https://doi.org/10.1039/D2SC02222B.

(34) De Gregorio, G. L.; Burdyny, T.; Loiudice, A.; Iyengar, P.; Smith, W. A.; Buonsanti, R. Facet-Dependent Selectivity of Cu Catalysts in Electrochemical CO2 Reduction at Commercially Viable Current Densities. *ACS Catal.* **2020**, *10* (9), 4854–4862. https://doi.org/10.1021/acscatal.0c00297.

(35) Tomboc, G. M.; Choi, S.; Kwon, T.; Hwang, Y. J.; Lee, K. Potential Link between Cu Surface and Selective CO2 Electroreduction: Perspective on Future Electrocatalyst Designs. *Advanced Materials* **2020**, *32* (17), 1908398. https://doi.org/10.1002/adma.201908398.

(36) Akter, T.; Pan, H.; Barile, C. J. Tandem Electrocatalytic CO2 Reduction inside a Membrane with Enhanced Selectivity for Ethylene. *J. Phys. Chem. C* **2022**. https://doi.org/10.1021/acs.jpcc.2c01663.

(37) Ozden, A.; Li, F.; Wang, Y.; Hung, S.-F.; Wang, X.; Chen, B.; Li, J.; Wicks, J.; Luo, M.; Wang, Z.; Agapie, T.; Peters, J. C.; Sargent, E. H.; Sinton, D. High-Rate and Efficient Ethylene Electrosynthesis Using a Catalyst:Promoter:Transport Layer. 46.

(38) Huang, M.; Gong, S.; Wang, C.; Yang, Y.; Jiang, P.; Wang, P.; Hu, L.; Chen, Q. Lewis-Basic EDTA as a Highly Active Molecular Electrocatalyst for CO2 Reduction to CH4. *Angewandte Chemie International Edition* **2021**, *60* (42), 23002–23009. https://doi.org/10.1002/anie.202110594.

(39) Banerjee, S.; Gerke, C. S.; Thoi, V. S. Guiding CO2RR Selectivity by Compositional Tuning in the Electrochemical Double Layer. *Acc. Chem. Res.* **2022**, *55* (4), 504–515. https://doi.org/10.1021/acs.accounts.1c00680.

(40) Nie, W.; Heim, G. P.; Watkins, N. B.; Agapie, T.; Peters, J. C. Organic Additive-Derived Films on Cu Electrodes Promote Electrochemical CO2 Reduction to C2+ Products Under Strongly Acidic Conditions. *Angewandte Chemie International Edition* **2023**, *62* (12), e202216102. https://doi.org/10.1002/anie.202216102.

(41) Han, Z.; Kortlever, R.; Chen, H.-Y.; Peters, J. C.; Agapie, T. CO $_2$ Reduction Selective for C $_{\geq 2}$ Products on Polycrystalline Copper with N-Substituted Pyridinium Additives. *ACS Cent. Sci.* **2017**, *3* (8), 853–859. https://doi.org/10.1021/acscentsci.7b00180.

(42) König, M.; Vaes, J.; Klemm, E.; Pant, D. Solvents and Supporting Electrolytes in the Electrocatalytic Reduction of CO2. *iScience* **2019**, *19*, 135–160. https://doi.org/10.1016/j.isci.2019.07.014.

(43) Moura de Salles Pupo, M.; Kortlever, R. Electrolyte Effects on the Electrochemical Reduction of CO $_2$. *ChemPhysChem* **2019**, *20* (22), 2926–2935. https://doi.org/10.1002/cphc.201900680.

(44) Deng, B.; Huang, M.; Zhao, X.; Mou, S.; Dong, F. Interfacial Electrolyte Effects on Electrocatalytic CO2 Reduction. *ACS Catal.* **2022**, *12* (1), 331–362. https://doi.org/10.1021/acscatal.1c03501.

(45) Marcandalli, G.; Monteiro, M. C. O.; Goyal, A.; Koper, M. T. M. Electrolyte Effects on CO2 Electrochemical Reduction to CO. *Acc. Chem. Res.* **2022**, *55* (14), 1900–1911. https://doi.org/10.1021/acs.accounts.2c00080.

(46) Shin, S.-J.; Choi, H.; Ringe, S.; Won, D. H.; Oh, H.-S.; Kim, D. H.; Lee, T.; Nam, D.-H.; Kim, H.; Choi, C. H. A Unifying Mechanism for Cation Effect Modulating C1 and C2 Productions from CO2 Electroreduction. May 11, 2022. https://doi.org/10.21203/rs.3.rs-1589012/v1.

(47) Verma, S.; Lu, X.; Ma, S.; Masel, R. I.; Kenis, P. J. A. The Effect of Electrolyte Composition on the Electroreduction of CO2 to CO on Ag Based Gas Diffusion Electrodes. *Phys. Chem. Chem. Phys.* **2016**, *18* (10), 7075–7084. https://doi.org/10.1039/C5CP05665A.

(48) Varela, A. S.; Ju, W.; Reier, T.; Strasser, P. Tuning the Catalytic Activity and Selectivity of Cu for CO2 Electroreduction in the Presence of Halides. *ACS Catal.* **2016**, *6* (4), 2136–2144. https://doi.org/10.1021/acscatal.5b02550.

(49) Tomisaki, M.; Kasahara, S.; Natsui, K.; Ikemiya, N.; Einaga, Y. Switchable Product Selectivity in the Electrochemical Reduction of Carbon Dioxide Using Boron-Doped Diamond Electrodes. *J. Am. Chem. Soc.* **2019**, *141* (18), 7414–7420. https://doi.org/10.1021/jacs.9b01773.

(50) Yoo, J. M.; Lukatskaya, M. R. *Anion Effect in Electrochemical CO2 Reduction: Enhanced Selectivity Enabled Through Anion Modulation*; preprint; Chemistry, 2023. https://doi.org/10.26434/chemrxiv-2023-8q0qt-v2.

(51) Suo, L.; Borodin, O.; Gao, T.; Olguin, M.; Ho, J.; Fan, X.; Luo, C.; Wang, C.; Xu, K. “Water-in-Salt” Electrolyte Enables High-Voltage Aqueous Lithium-Ion Chemistries. *Science* **2015**, *350* (6263), 938–943. https://doi.org/10.1126/science.aab1595.

(52) Amiri, M.; Bélanger, D. Physicochemical and Electrochemical Characterization of Salt-in-Water and Water-in-Salt Potassium and Lithium Acetate Electrolytes. *Journal of Materials Chemistry A* **2021**, *9* (42), 24012–24023. https://doi.org/10.1039/D1TA07214E.

(53) Zhao, Y.; Hu, X.; Stucky, G. D.; Boettcher, S. W. Thermodynamic, Kinetic, and Transport Contributions to Hydrogen Evolution Activity and Electrolyte-Stability Windows for Water-in-Salt Electrolytes. *Journal of the American Chemical Society* **2024**. https://doi.org/10.1021/jacs.3c12980.

(54) Xiao, D.; Zhang, L.; Li, Z.; Dou, H.; Zhang, X. Design Strategies and Research Progress for Water-in-Salt Electrolytes. *Energy Storage Materials* **2022**, *44*, 10–28. https://doi.org/10.1016/j.ensm.2021.09.035.

(55) Dong, Q.; Zhang, X.; He, D.; Lang, C.; Wang, D. Role of H2O in CO2 Electrochemical Reduction As Studied in a Water-in-Salt System. *ACS Central Science* **2019**, 7.

(56) Ren, W.; Xu, A.; Chan, K.; Hu, X. A Cation Concentration Gradient Approach to Tune the Selectivity and Activity of CO2 Electroreduction. *Angewandte Chemie International Edition* **2022**, *61* (49), e202214173. https://doi.org/10.1002/anie.202214173.

(57) Zhang, H.; Gao, J.; Raciti, D.; Hall, A. S. Promoting Cu-Catalysed CO2 Electroreduction to Multicarbon Products by Tuning the Activity of H2O. *Nat Catal* **2023**, *6* (9), 807–817. https://doi.org/10.1038/s41929-023-01010-6.

(58) Murata, A.; Hori, Y. Product Selectivity Affected by Cationic Species in Electrochemical Reduction of CO2 and CO at a Cu Electrode. *BCSJ* **1991**, *64* (1), 123–127. https://doi.org/10.1246/bcsj.64.123.

(59) Liu, T.; Tang, L.; Luo, H.; Cheng, S.; Liu, M. A Promising Water-in-Salt Electrolyte for Aqueous Based Electrochemical Energy Storage Cells with a Wide Potential Window: Highly Concentrated HCOOK. *Chem. Commun.* **2019**, *55* (85), 12817–12820. https://doi.org/10.1039/C9CC05927J.

(60) Lees, E. W.; Mowbray, B. A. W.; Parlane, F. G. L.; Berlinguette, C. P. Gas Diffusion Electrodes and Membranes for CO2 Reduction Electrolysers. *Nat Rev Mater* **2022**, *7* (1), 55–64. https://doi.org/10.1038/s41578-021-00356-2.

(61) Nguyen, T. N.; Dinh, C.-T. Gas Diffusion Electrode Design for Electrochemical Carbon Dioxide Reduction. *Chem. Soc. Rev.* **2020**, *49* (21), 7488–7504. https://doi.org/10.1039/D0CS00230E.

(62) Rabiee, H.; Ge, L.; Zhang, X.; Hu, S.; Li, M.; Yuan, Z. Gas Diffusion Electrodes (GDEs) for Electrochemical Reduction of Carbon Dioxide, Carbon Monoxide, and Dinitrogen to Value-Added Products: A Review. *Energy Environ. Sci.* **2021**, *14* (4), 1959–2008. https://doi.org/10.1039/D0EE03756G.

(63) Möller, T.; Ngo Thanh, T.; Wang, X.; Ju, W.; Jovanov, Z.; Strasser, P. The Product Selectivity Zones in Gas Diffusion Electrodes during the Electrocatalytic Reduction of CO_2. *Energy Environ. Sci.* **2021**, *14* (11), 5995–6006. https://doi.org/10.1039/D1EE01696B.

(64) Tan, Y. C.; Lee, K. B.; Song, H.; Oh, J. Modulating Local CO2 Concentration as a General Strategy for Enhancing C−C Coupling in CO2 Electroreduction. *Joule* **2020**, *4* (5), 1104–1120. https://doi.org/10.1016/j.joule.2020.03.013.

(65) Song, H.; Song, J. T.; Kim, B.; Tan, Y. C.; Oh, J. Activation of C2H4 Reaction Pathways in Electrochemical CO2 Reduction under Low CO2 Partial Pressure. *Applied Catalysis B: Environmental* **2020**, *272*, 119049. https://doi.org/10.1016/j.apcatb.2020.119049.

(66) Li, J.; Wang, Z.; McCallum, C.; Xu, Y.; Li, F.; Wang, Y.; Gabardo, C. M.; Dinh, C.-T.; Zhuang, T.-T.; Wang, L.; Howe, J. Y.; Ren, Y.; Sargent, E. H.; Sinton, D. Constraining CO Coverage on Copper Promotes High-Efficiency Ethylene Electroproduction. *Nat Catal* **2019**, *2* (12), 1124–1131. https://doi.org/10.1038/s41929-019-0380-x.

(67) Moradzaman, M.; Mul, G. Optimizing CO Coverage on Rough Copper Electrodes: Effect of the Partial Pressure of CO and Electrolyte Anions (pH) on Selectivity toward Ethylene. *J. Phys. Chem. C* **2021**, *125* (12), 6546–6554. https://doi.org/10.1021/acs.jpcc.0c10792.

(68) Henckel, D. A.; Counihan, M. J.; Holmes, H. E.; Chen, X.; Nwabara, U. O.; Verma, S.; Rodríguez-López, J.; Kenis, P. J. A.; Gewirth, A. A. Potential Dependence of the Local pH in a CO $_2$ Reduction Electrolyzer. *ACS Catal.* **2021**, *11* (1), 255–263. https://doi.org/10.1021/acscatal.0c04297.

(69) Monteiro, M. C. O.; Koper, M. T. M. Measuring Local pH in Electrochemistry. *Current Opinion in Electrochemistry* **2021**, *25*, 100649. https://doi.org/10.1016/j.coelec.2020.100649.

(70) Yang, K.; Kas, R.; Smith, W. A. In Situ Infrared Spectroscopy Reveals Persistent Alkalinity near Electrode Surfaces during CO $_2$ Electroreduction. *J. Am. Chem. Soc.* **2019**, *141* (40), 15891–15900. https://doi.org/10.1021/jacs.9b07000.

(71) Yao, K.; Li, J.; Wang, H.; Lu, R.; Yang, X.; Luo, M.; Wang, N.; Wang, Z.; Liu, C.; Jing, T.; Chen, S.; Cortés, E.; Maier, S. A.; Zhang, S.; Li, T.; Yu, Y.; Liu, Y.; Kang, X.; Liang, H. Mechanistic Insights into OC–COH Coupling in CO2 Electroreduction on Fragmented Copper. *J. Am. Chem. Soc.* **2022**, *144* (31), 14005–14011. https://doi.org/10.1021/jacs.2c01044.

(72) Sandberg, R. B.; Montoya, J. H.; Chan, K.; Nørskov, J. K. CO-CO Coupling on Cu Facets: Coverage, Strain and Field Effects. *Surface Science* **2016**, *654*, 56–62. https://doi.org/10.1016/j.susc.2016.08.006.

(73) Xiao, H.; Cheng, T.; Goddard, W. A.; Sundararaman, R. Mechanistic Explanation of the pH Dependence and Onset Potentials for Hydrocarbon Products from Electrochemical Reduction of CO on Cu (111). *J. Am. Chem. Soc.* **2016**, *138* (2), 483–486. https://doi.org/10.1021/jacs.5b11390.

(74) Pérez-Gallent, E.; Figueiredo, M. C.; Calle-Vallejo, F.; Koper, M. T. M. Spectroscopic Observation of a Hydrogenated CO Dimer Intermediate During CO Reduction on Cu(100) Electrodes. *Angewandte Chemie International Edition* **2017**, *56* (13), 3621–3624. https://doi.org/10.1002/anie.201700580.

(75) Xiao, H.; Goddard, W. A.; Cheng, T.; Liu, Y. Cu Metal Embedded in Oxidized Matrix Catalyst to Promote CO2 Activation and CO Dimerization for Electrochemical Reduction of CO2. *Proceedings of the National Academy of Sciences* **2017**, *114* (26), 6685–6688. https://doi.org/10.1073/pnas.1702405114.

(76) Kim, Y.; Park, S.; Shin, S.-J.; Choi, W.; Koun Min, B.; Kim, H.; Kim, W.; Jeong Hwang, Y. Time-Resolved Observation of C–C Coupling Intermediates on Cu Electrodes for Selective Electrochemical CO 2 Reduction. *Energy & Environmental Science* **2020**, *13* (11), 4301–4311. https://doi.org/10.1039/D0EE01690J.

(77) Wang, L.; Nitopi, S. A.; Bertheussen, E.; Orazov, M.; Morales-Guio, C. G.; Liu, X.; Higgins, D. C.; Chan, K.; Nørskov, J. K.; Hahn, C.; Jaramillo, T. F. Electrochemical Carbon Monoxide Reduction on Polycrystalline Copper: Effects of Potential, Pressure, and pH on Selectivity toward Multicarbon and Oxygenated Products. *ACS Catal.* **2018**, *8* (8), 7445–7454. https://doi.org/10.1021/acscatal.8b01200.

(78) Hori, Y.; Takahashi, R.; Yoshinami, Y.; Murata, A. Electrochemical Reduction of CO at a Copper Electrode. *J. Phys. Chem. B* **1997**, *101* (36), 7075–7081. https://doi.org/10.1021/jp970284i.

(79) Dinh, C.-T.; Burdyny, T.; Kibria, M. G.; Seifitokaldani, A.; Gabardo, C. M.; García de Arquer, F. P.; Kiani, A.; Edwards, J. P.; De Luna, P.; Bushuyev, O. S.; Zou, C.; Quintero-Bermudez, R.; Pang, Y.; Sinton, D.; Sargent, E. H. CO2 Electroreduction to Ethylene via Hydroxide-Mediated Copper Catalysis at an Abrupt Interface. *Science* **2018**, *360* (6390), 783–787. https://doi.org/10.1126/science.aas9100.

(80) Varela, A. S.; Kroschel, M.; Reier, T.; Strasser, P. Controlling the Selectivity of CO2 Electroreduction on Copper: The Effect of the Electrolyte Concentration and the Importance of the Local pH. *Catalysis Today* **2016**, *260*, 8–13. https://doi.org/10.1016/j.cattod.2015.06.009.

(81) Welch, A. J.; Fenwick, A. Q.; Böhme, A.; Chen, H.-Y.; Sullivan, I.; Li, X.; DuChene, J. S.; Xiang, C.; Atwater, H. A. Operando Local pH Measurement within Gas Diffusion Electrodes Performing Electrochemical Carbon Dioxide Reduction. *J. Phys. Chem. C* **2021**, *125* (38), 20896–20904. https://doi.org/10.1021/acs.jpcc.1c06265.

(82) Böhme, A.; Bui, J. C.; Fenwick, A. Q.; Bhide, R.; Feltenberger, C. N.; Welch, A. J.; King, A. J.; Bell, A. T.; Weber, A. Z.; Ardo, S.; Atwater, H. A. Direct Observation of the Local Microenvironment in Inhomogeneous CO2 Reduction Gas Diffusion Electrodes via Versatile pOH Imaging. *Energy Environ. Sci.* **2023**, *16* (4), 1783–1795. https://doi.org/10.1039/D2EE02607D.

(83) Dolmanan, S. B.; Böhme, A.; Fan, Z.; King, A. J.; Fenwick, A. Q.; Handoko, A. D.; Leow, W. R.; Weber, A. Z.; Ma, X.; Khoo, E.; Atwater, H. A.; Lum, Y. Local Microenvironment Tuning Induces Switching between Electrochemical CO2 Reduction Pathways. *J. Mater. Chem. A* **2023**, *11* (25), 13493–13501. https://doi.org/10.1039/D3TA02558F.

(84) Ringe, S.; Clark, E. L.; Resasco, J.; Walton, A.; Seger, B.; Bell, A. T.; Chan, K. Understanding Cation Effects in Electrochemical CO2 Reduction. *Energy Environ. Sci.* **2019**, *12* (10), 3001–3014. https://doi.org/10.1039/C9EE01341E.

(85) Monteiro, M. C. O.; Dattila, F.; Hagedoorn, B.; García-Muelas, R.; López, N.; Koper, M. T. M. Absence of CO2 Electroreduction on Copper, Gold and Silver Electrodes without Metal Cations in Solution. *Nat Catal* **2021**, *4* (8), 654–662. https://doi.org/10.1038/s41929-021-00655-5.

(86) Park, D.; Jung, Y. Atomic-Scale Understanding of Alkali Metal Cation Effects on Electro-Catalytic Reactions. *Chem Catalysis* **2023**, 100823. https://doi.org/10.1016/j.checat.2023.100823.

(87) Cheng, T.; Xiao, H.; Goddard, W. A. Full Atomistic Reaction Mechanism with Kinetics for CO Reduction on Cu(100) from Ab Initio Molecular Dynamics Free-Energy Calculations at 298 K. *Proceedings of the National Academy of Sciences* **2017**, *114* (8), 1795–1800. https://doi.org/10.1073/pnas.1612106114.

(88) Gao, D.; Scholten, F.; Roldan Cuenya, B. Improved CO2 Electroreduction Performance on Plasma-Activated Cu Catalysts via Electrolyte Design: Halide Effect. *ACS Catal.* **2017**, *7* (8), 5112–5120. https://doi.org/10.1021/acscatal.7b01416.

(89) Gao, D.; Sinev, I.; Scholten, F.; Arán-Ais, R. M.; Divins, N. J.; Kvashnina, K.; Timoshenko, J.; Roldan Cuenya, B. Selective CO2 Electroreduction to Ethylene and Multicarbon Alcohols via Electrolyte-Driven Nanostructuring. *Angewandte Chemie International Edition* **2019**, *58* (47), 17047–17053. https://doi.org/10.1002/anie.201910155.

(90) Yuan, T.; Wang, T.; Zhang, G.; Deng, W.; Cheng, D.; Gao, H.; Zhao, J.; Yu, J.; Zhang, P.; Gong, J. The Effect of Specific Adsorption of Halide Ions on Electrochemical CO2 Reduction. *Chem. Sci.* **2022**, *13* (27), 8117–8123. https://doi.org/10.1039/D2SC02689A.

(91) Huang, Y.; Ong, C. W.; Yeo, B. S. Effects of Electrolyte Anions on the Reduction of Carbon Dioxide to Ethylene and Ethanol on Copper (100) and (111) Surfaces. *ChemSusChem* **2018**, *11* (18), 3299–3306. https://doi.org/10.1002/cssc.201801078.

(92) Biesinger, M. C. Advanced Analysis of Copper X-Ray Photoelectron Spectra. *Surface and Interface Analysis* **2017**, *49* (13), 1325–1334. https://doi.org/10.1002/sia.6239.

(93) Martin, L.; Martinez, H.; Poinot, D.; Pecquenard, B.; Le Cras, F. Comprehensive X-Ray Photoelectron Spectroscopy Study of the Conversion Reaction Mechanism of CuO in Lithiated Thin Film Electrodes. *J. Phys. Chem. C* **2013**, *117* (9), 4421–4430. https://doi.org/10.1021/jp3119633.

(94) Jiang, P.; Prendergast, D.; Borondics, F.; Porsgaard, S.; Giovanetti, L.; Pach, E.; Newberg, J.; Bluhm, H.; Besenbacher, F.; Salmeron, M. Experimental and Theoretical Investigation of the Electronic Structure of Cu2O and CuO Thin Films on Cu(110) Using x-Ray Photoelectron and Absorption Spectroscopy. *The Journal of Chemical Physics* **2013**, *138* (2), 024704. https://doi.org/10.1063/1.4773583.

(95) Biesinger, M. C.; Lau, L. W. M.; Gerson, A. R.; Smart, R. St. C. Resolving Surface Chemical States in XPS Analysis of First Row Transition Metals, Oxides and Hydroxides: Sc, Ti, V, Cu and Zn. *Applied Surface Science* **2010**, *257* (3), 887–898. https://doi.org/10.1016/j.apsusc.2010.07.086.

(96) Wang, L.; Nitopi, S.; Wong, A. B.; Snider, J. L.; Nielander, A. C.; Morales-Guio, C. G.; Orazov, M.; Higgins, D. C.; Hahn, C.; Jaramillo, T. F. Electrochemically Converting Carbon Monoxide to Liquid Fuels by Directing Selectivity with Electrode Surface Area. *Nat Catal* **2019**, *2* (8), 702–708. https://doi.org/10.1038/s41929-019-0301-z.

(97) Wang, X.; Klingan, K.; Klingenhof, M.; Möller, T.; Ferreira de Araújo, J.; Martens, I.; Bagger, A.; Jiang, S.; Rossmeisl, J.; Dau, H.; Strasser, P. Morphology and Mechanism of Highly Selective Cu(II) Oxide Nanosheet Catalysts for Carbon Dioxide Electroreduction. *Nat Commun* **2021**, *12* (1), 794. https://doi.org/10.1038/s41467-021-20961-7.

(98) Yang, Y.; Louisia, S.; Yu, S.; Jin, J.; Roh, I.; Chen, C.; Fonseca Guzman, M. V.; Feijóo, J.; Chen, P.-C.; Wang, H.; Pollock, C. J.; Huang, X.; Shao, Y.-T.; Wang, C.; Muller, D. A.; Abruña, H. D.; Yang, P. Operando Studies Reveal Active Cu Nanograins for CO2 Electroreduction. *Nature* **2023**, *614* (7947), 262–269. https://doi.org/10.1038/s41586-022-05540-0.

(99) Grosse, P.; Yoon, A.; Rettenmaier, C.; Herzog, A.; Chee, S. W.; Roldan Cuenya, B. Dynamic Transformation of Cubic Copper Catalysts during CO2 Electroreduction and Its Impact on Catalytic Selectivity. *Nat Commun* **2021**, *12* (1), 6736. https://doi.org/10.1038/s41467-021-26743-5.

(100) Arán-Ais, R. M.; Rizo, R.; Grosse, P.; Algara-Siller, G.; Dembélé, K.; Plodinec, M.; Lunkenbein, T.; Chee, S. W.; Cuenya, B. R. Imaging Electrochemically Synthesized Cu2O Cubes and Their Morphological Evolution under Conditions Relevant to CO2 Electroreduction. *Nat Commun* **2020**, *11* (1), 3489. https://doi.org/10.1038/s41467-020-17220-6.

(101) Kas, R.; Yang, K.; Bohra, D.; Kortlever, R.; Burdyny, T.; Smith, W. A. Electrochemical CO $_2$ Reduction on Nanostructured Metal Electrodes: Fact or Defect? *Chem. Sci.* **2020**, *11* (7), 1738–1749. https://doi.org/10.1039/C9SC05375A.

(102) Gunathunge, C. M.; Li, J.; Li, X.; Waegele, M. M. Surface-Adsorbed CO as an Infrared Probe of Electrocatalytic Interfaces. *ACS Catal.* **2020**, *10* (20), 11700–11711. https://doi.org/10.1021/acscatal.0c03316.

(103) Elderderi, S.; Leman-Loubière, C.; Wils, L.; Henry, S.; Bertrand, D.; Byrne, H. J.; Chourpa, I.; Enguehard-Gueiffier, C.; Munnier, E.; Elbashir, A. A.; Boudesocque-Delaye, L.; Bonnier, F. ATR-IR Spectroscopy for Rapid Quantification of Water Content in Deep Eutectic Solvents. *Journal of Molecular Liquids* **2020**, *311*, 113361. https://doi.org/10.1016/j.molliq.2020.113361.

(104) Mojet, B.; Ebbesen, S.; Lefferts, L. ChemInform Abstract: Light at the Interface: The Potential of Attenuated Total Reflection Infrared Spectroscopy for Understanding Heterogeneous Catalysis in Water. *Chemical Society reviews* **2010**, *39*, 4643–4655. https://doi.org/10.1039/c0cs00014k.

(105) Gunathunge, C. M.; Li, J.; Li, X.; Waegele, M. M. Surface-Adsorbed CO as an Infrared Probe of Electrocatalytic Interfaces. *ACS Catal.* **2020**, *10* (20), 11700–11711. https://doi.org/10.1021/acscatal.0c03316.

(106) Bai, H.; Cheng, T.; Li, S.; Zhou, Z.; Yang, H.; Li, J.; Xie, M.; Ye, J.; Ji, Y.; Li, Y.; Zhou, Z.; Sun, S.; Zhang, B.; Peng, H. Controllable CO Adsorption Determines Ethylene and Methane Productions from CO2 Electroreduction. *Science Bulletin* **2021**, *66* (1), 62–68. https://doi.org/10.1016/j.scib.2020.06.023.

(107) Gunathunge, C. M.; Ovalle, V. J.; Li, Y.; Janik, M. J.; Waegele, M. M. Existence of an Electrochemically Inert CO Population on Cu Electrodes in Alkaline pH. *ACS Catal.* **2018**, *8* (8), 7507–7516. https://doi.org/10.1021/acscatal.8b01552.

(108) Rebstock, J. A.; Zhu, Q.; Baker, L. R. Comparing Interfacial Cation Hydration at Catalytic Active Sites and Spectator Sites on Gold Electrodes: Understanding Structure Sensitive CO2 Reduction Kinetics. *Chem. Sci.* **2022**, *13* (25), 7634–7643. https://doi.org/10.1039/D2SC01878K.

(109) Lee, S. Y.; Kim, J.; Bak, G.; Lee, E.; Kim, D.; Yoo, S.; Kim, J.; Yun, H.; Hwang, Y. J. Probing Cation Effects on *CO Intermediates from Electroreduction of CO2 through Operando Raman Spectroscopy. *J. Am. Chem. Soc.* **2023**, *145* (42), 23068–23075. https://doi.org/10.1021/jacs.3c05799.

(110) Nesbitt, N. T.; Burdyny, T.; Simonson, H.; Salvatore, D.; Bohra, D.; Kas, R.; Smith, W. A. Liquid–Solid Boundaries Dominate Activity of CO2 Reduction on Gas-Diffusion Electrodes. *ACS Catal.* **2020**, *10* (23), 14093–14106. https://doi.org/10.1021/acscatal.0c03319.

(111) Zhan, C.; Dattila, F.; Rettenmaier, C.; Bergmann, A.; Kühl, S.; García-Muelas, R.; López, N.; Cuenya, B. R. Revealing the CO Coverage-Driven C–C Coupling Mechanism for Electrochemical CO2 Reduction on Cu2O Nanocubes via Operando Raman Spectroscopy. *ACS Catal.* **2021**, *11* (13), 7694–7701. https://doi.org/10.1021/acscatal.1c01478.

(112) Chou, T.-C.; Chang, C.-C.; Yu, H.-L.; Yu, W.-Y.; Dong, C.-L.; Velasco-Vélez, J.-J.; Chuang, C.-H.; Chen, L.-C.; Lee, J.-F.; Chen, J.-M.; Wu, H.-L. Controlling the Oxidation State of the Cu Electrode and Reaction Intermediates for Electrochemical CO2 Reduction to Ethylene. *J. Am. Chem. Soc.* **2020**, *142* (6), 2857–2867. https://doi.org/10.1021/jacs.9b11126.

(113) Ovalle, V. J.; Waegele, M. M. Impact of Electrolyte Anions on the Adsorption of CO on Cu Electrodes. *J. Phys. Chem. C* **2020**, *124* (27), 14713–14721. https://doi.org/10.1021/acs.jpcc.0c04037.

(114) Mohandas, N.; Narayanan, T. N.; Cuesta, A. Tailoring the Interfacial Water Structure by Electrolyte Engineering for Selective Electrocatalytic Reduction of Carbon Dioxide. *ACS Catal.* **2023**, *13* (13), 8384–8393. https://doi.org/10.1021/acscatal.3c01223.

(115) Wang, Y.-H.; Zheng, S.; Yang, W.-M.; Zhou, R.-Y.; He, Q.-F.; Radjenovic, P.; Dong, J.-C.; Li, S.; Zheng, J.; Yang, Z.-L.; Attard, G.; Pan, F.; Tian, Z.-Q.; Li, J.-F. In Situ Raman Spectroscopy Reveals the Structure and Dissociation of Interfacial Water. *Nature* **2021**, *600* (7887), 81–85. https://doi.org/10.1038/s41586-021-04068-z.

(116) Ataka, K.; Yotsuyanagi, T.; Osawa, M. Potential-Dependent Reorientation of Water Molecules at an Electrode/Electrolyte Interface Studied by Surface-Enhanced Infrared Absorption Spectroscopy. *J. Phys. Chem.* **1996**, *100* (25), 10664–10672. https://doi.org/10.1021/jp953636z.

(117) Bhattacharyya, D.; E. Videla, P.; Cattaneo, M.; S. Batista, V.; Lian, T.; P. Kubiak, C. Vibrational Stark Shift Spectroscopy of Catalysts under the Influence of Electric Fields at Electrode–Solution Interfaces. *Chemical Science* **2021**, *12* (30), 10131–10149. https://doi.org/10.1039/D1SC01876K.

(118) Ringe, S.; Clark, E. L.; Resasco, J.; Walton, A.; Seger, B.; Bell, A. T.; Chan, K. Understanding Cation Effects in Electrochemical CO2 Reduction. *Energy Environ. Sci.* **2019**, *12* (10), 3001–3014. https://doi.org/10.1039/C9EE01341E.

(119) Malkani, A. S.; Li, J.; Oliveira, N. J.; He, M.; Chang, X.; Xu, B.; Lu, Q. Understanding the Electric and Nonelectric Field Components of the Cation Effect on the Electrochemical CO Reduction Reaction. *Science Advances* **2020**, *6* (45), eabd2569. https://doi.org/10.1126/sciadv.abd2569.

(120) Sartin, M. M.; Yu, Z.; Chen, W.; He, F.; Sun, Z.; Chen, Y.-X.; Huang, W. Effect of Particle Shape and Electrolyte Cation on CO Adsorption to Copper Oxide Nanoparticle Electrocatalysts. *J. Phys. Chem. C* **2018**, *122* (46), 26489–26498. https://doi.org/10.1021/acs.jpcc.8b08541.

(121) Woodruff, D. P.; Hayden, B. E.; Prince, K.; Bradshaw, A. M. Dipole Coupling and Chemical Shifts in IRAS of CO Adsorbed on Cu(110). *Surface Science* **1982**, *123* (2), 397–412. https://doi.org/10.1016/0039-6028(82)90336-3.

(122) Chang, X.; Xiong, H.; Xu, Y.; Zhao, Y.; Lu, Q.; Xu, B. Determining Intrinsic Stark Tuning Rates of Adsorbed CO on Copper Surfaces. *Catal. Sci. Technol.* **2021**, *11* (20), 6825–6831. https://doi.org/10.1039/D1CY01090E.

(123) Gameel, K. M.; Sharafeldin, I. M.; Abourayya, A. U.; Biby, A. H.; Allam, N. K. Unveiling CO Adsorption on Cu Surfaces: New Insights from Molecular Orbital Principles. *Phys. Chem. Chem. Phys.* **2018**, *20* (40), 25892–25900. https://doi.org/10.1039/C8CP04253E.

(124) Blyholder, G. Molecular Orbital View of Chemisorbed Carbon Monoxide. *J. Phys. Chem.* **1964**, *68* (10), 2772–2777. https://doi.org/10.1021/j100792a006.

(125) Banerji, L. C.; Jang, H.; Gardner, A. M.; Cowan, A. J. Studying the Cation Dependence of CO2 Reduction Intermediates at Cu by in Situ VSFG Spectroscopy. *Chem. Sci.* **2024**, *15* (8), 2889–2897. https://doi.org/10.1039/D3SC05295H.

(126) Uddin, J.; Anderson, A. B. Trends with Coverage and pH in Stark Tuning Rates for CO on Pt(1 1 1) Electrodes. *Electrochimica Acta* **2013**, *108*, 398–403. https://doi.org/10.1016/j.electacta.2013.06.088.

(127) Avilés Acosta, J. E.; Lin, J. C.; Un Lee, D.; Jaramillo, T. F.; Hahn, C. Electrochemical Flow Reactor Design Allows Tunable Mass Transport Conditions for Operando Surface Enhanced Infrared Absorption Spectroscopy. *ChemCatChem* **2023**, *15* (15), e202300520. https://doi.org/10.1002/cctc.202300520.

(128) Falk, M.; Miller, A. G. Infrared Spectrum of Carbon Dioxide in Aqueous Solution. *Vibrational Spectroscopy* **1992**, *4* (1), 105–108. https://doi.org/10.1016/0924-2031(92)87018-B.

(129) Miyake, H.; Ye, S.; Osawa, M. Electroless Deposition of Gold Thin Films on Silicon for Surface-Enhanced Infrared Spectroelectrochemistry. *Electrochemistry Communications* **2002**, *4* (12), 973–977. https://doi.org/10.1016/S1388-2481(02)00510-6.

(130) Heyes, J.; Dunwell, M.; Xu, B. CO2 Reduction on Cu at Low Overpotentials with Surface-Enhanced in Situ Spectroscopy. *J. Phys. Chem. C* **2016**, *120* (31), 17334–17341. https://doi.org/10.1021/acs.jpcc.6b03065.

(131) Jo, S.; Kim, T.; Iyer, V. G.; Im, W. CHARMM-GUI: A Web-Based Graphical User Interface for CHARMM. *Journal of Computational Chemistry* **2008**, *29* (11), 1859–1865. https://doi.org/10.1002/jcc.20945.

(132) Choi, Y. K.; Kern, N. R.; Kim, S.; Kanhaiya, K.; Afshar, Y.; Jeon, S. H.; Jo, S.; Brooks, B. R.; Lee, J.; Tadmor, E. B.; Heinz, H.; Im, W. CHARMM-GUI Nanomaterial Modeler for Modeling and Simulation of Nanomaterial Systems. *J. Chem. Theory Comput.* **2022**, *18* (1), 479–493. https://doi.org/10.1021/acs.jctc.1c00996.

(133) Abraham, M. J.; Murtola, T.; Schulz, R.; Páll, S.; Smith, J. C.; Hess, B.; Lindahl, E. GROMACS: High Performance Molecular Simulations through Multi-Level Parallelism from Laptops to Supercomputers. *SoftwareX* **2015**, *1–2*, 19–25. https://doi.org/10.1016/j.softx.2015.06.001.

(134) Lee, J.; Cheng, X.; Jo, S.; MacKerell, A. D.; Klauda, J. B.; Im, W. CHARMM-GUI Input Generator for NAMD, Gromacs, Amber, Openmm, and CHARMM/OpenMM Simulations Using the CHARMM36 Additive Force Field. *Biophysical Journal* **2016**, *110* (3), 641a. https://doi.org/10.1016/j.bpj.2015.11.3431.

(135) Jorgensen, W. L.; Chandrasekhar, J.; Madura, J. D.; Impey, R. W.; Klein, M. L. Comparison of Simple Potential Functions for Simulating Liquid Water. *The Journal of Chemical Physics* **1983**, *79* (2), 926–935. https://doi.org/10.1063/1.445869.

(136) Bussi, G.; Donadio, D.; Parrinello, M. Canonical Sampling through Velocity Rescaling. *The Journal of Chemical Physics* **2007**, *126* (1), 014101. https://doi.org/10.1063/1.2408420.

(137) Kresse, G.; Furthmüller, J. Efficient Iterative Schemes for Ab Initio Total-Energy Calculations Using a Plane-Wave Basis Set. *Phys. Rev. B* **1996**, *54* (16), 11169–11186. https://doi.org/10.1103/PhysRevB.54.11169.

(138) Perdew, J. P.; Burke, K.; Ernzerhof, M. Generalized Gradient Approximation Made Simple. *Phys. Rev. Lett.* **1996**, *77* (18), 3865–3868. https://doi.org/10.1103/PhysRevLett.77.3865.

(139) Johnson, E. R.; Becke, A. D. A Post-Hartree-Fock Model of Intermolecular Interactions: Inclusion of Higher-Order Corrections. *The Journal of Chemical Physics* **2006**, *124* (17), 174104. https://doi.org/10.1063/1.2190220.

(140) Blöchl, P. E. Projector Augmented-Wave Method. *Phys. Rev. B* **1994**, *50* (24), 17953–17979. https://doi.org/10.1103/PhysRevB.50.17953.

(141) Nosé, S. A Unified Formulation of the Constant Temperature Molecular Dynamics Methods. *The Journal of Chemical Physics* **1984**, *81* (1), 511–519. https://doi.org/10.1063/1.447334.

(142) Hoover, W. G. Canonical Dynamics: Equilibrium Phase-Space Distributions. *Phys. Rev. A* **1985**, *31* (3), 1695–1697. https://doi.org/10.1103/PhysRevA.31.1695.

(143) Mathew, K.; Kolluru, V. S. C.; Mula, S.; Steinmann, S. N.; Hennig, R. G. Implicit Self-Consistent Electrolyte Model in Plane-Wave Density-Functional Theory. *The Journal of Chemical Physics* **2019**, *151* (23), 234101. https://doi.org/10.1063/1.5132354.

(144) Le, D. An Explicit-Implicit Hybrid Solvent Model for Grand Canonical Simulations of the Electrochemical Environment. ChemRxiv March 27, 2023. https://doi.org/10.26434/chemrxiv-2023-z2n4n.

(145) Laio, A.; Parrinello, M. Escaping Free-Energy Minima. *Proceedings of the National Academy of Sciences* **2002**, *99* (20), 12562–12566. https://doi.org/10.1073/pnas.202427399.

(146) Lin, S.-T.; Maiti, P. K.; Goddard, W. A. I. Two-Phase Thermodynamic Model for Efficient and Accurate Absolute Entropy of Water from Molecular Dynamics Simulations. *J. Phys. Chem. B* **2010**, *114* (24), 8191–8198. https://doi.org/10.1021/jp103120q.

(147) Wuttig, A.; Liu, C.; Peng, Q.; Yaguchi, M.; Hendon, C. H.; Motobayashi, K.; Ye, S.; Osawa, M.; Surendranath, Y. Tracking a Common Surface-Bound Intermediate during CO2-to-Fuels Catalysis. *ACS Cent. Sci.* **2016**, *2* (8), 522–528. https://doi.org/10.1021/acscentsci.6b00155.

(148) Roiaz, M.; Falivene, L.; Rameshan, C.; Cavallo, L.; Kozlov, S. M.; Rupprechter, G. Roughening of Copper (100) at Elevated CO Pressure: Cu Adatom and Cluster Formation Enable CO Dissociation. *J. Phys. Chem. C* **2019**, *123* (13), 8112–8121. https://doi.org/10.1021/acs.jpcc.8b07668.

(149) Feibelman, P. J.; Hammer, B.; Nørskov, J. K.; Wagner, F.; Scheffler, M.; Stumpf, R.; Watwe, R.; Dumesic, J. The CO/Pt(111) Puzzle. *J. Phys. Chem. B* **2001**, *105* (18), 4018–4025. https://doi.org/10.1021/jp002302t.

(150) Kresse, G.; Gil, A.; Sautet, P. Significance of Single-Electron Energies for the Description of CO on Pt(111). *Phys. Rev. B* **2003**, *68* (7), 073401. https://doi.org/10.1103/PhysRevB.68.073401.

(151) Gajdoš, M.; Hafner, J. CO Adsorption on Cu(1 1 1) and Cu(0 0 1) Surfaces: Improving Site Preference in DFT Calculations. *Surface Science* **2005**, *590* (2), 117–126. https://doi.org/10.1016/j.susc.2005.04.047.

(152) Hu, Q.-M.; Reuter, K.; Scheffler, M. Towards an Exact Treatment of Exchange and Correlation in Materials: Application to the ``CO Adsorption Puzzle'' and Other Systems. *Phys. Rev. Lett.* **2007**, *98* (17), 176103. https://doi.org/10.1103/PhysRevLett.98.176103.

(153) Stroppa, A.; Termentzidis, K.; Paier, J.; Kresse, G.; Hafner, J. CO Adsorption on Metal Surfaces: A Hybrid Functional Study with Plane-Wave Basis Set. *Phys. Rev. B* **2007**, *76* (19), 195440. https://doi.org/10.1103/PhysRevB.76.195440.

(154) Chen, Z.; Liu, Z.; Xu, X. Accurate Descriptions of Molecule-Surface Interactions in Electrocatalytic CO2 Reduction on the Copper Surfaces. *Nat Commun* **2023**, *14* (1), 936. https://doi.org/10.1038/s41467-023-36695-7.